THE GEOLOGICAL SOCIETY OF AMERICA®

Apatite records metamorphic and hydrothermal fluid evolution at the large Shuangqishan orogenic gold deposit, SE China

Ying Ma[1], Shao-Yong Jiang[1,†], and Hartwig E. Frimmel[2,3]

[1]*State Key Laboratory of Geological Processes and Mineral Resources, School of Earth Resources, Collaborative Innovation Center for Exploration of Strategic Mineral Resources, China University of Geosciences, Wuhan 430074, P.R. China*

[2]*Bavarian Georesources Center, Department of Geodynamics and Geomaterials Research, Institute of Geography and Geology, University of Würzburg, Am Hubland, Würzburg 97074, Germany*

[3]*Department of Geological Sciences, University of Cape Town, Rondebosch 7700, South Africa*

ABSTRACT

Orogenic gold deposits are currently the world's major source of Au, but uncertainty exists in the timing of mineralization relative to the ages of host rocks, metamorphism, and magmatism. Consequently, the origin and detailed evolution of ore-forming fluids have long been elusive. Apatite occurs widespread in various types of mineral deposits and can provide valuable information on ore genesis. Here, we present textural, high-precision in situ U-Pb geochronological, trace elements, and Sr isotope data for metamorphic and hydrothermal apatite in the Shuangqishan gold deposit in southeastern China. These data, together with U-Pb dates of metavolcanic host rocks, granitic and mafic intrusive rocks, allow us to precisely constrain the timing of mineralization and reconstruct the history of the ore-forming fluids there. The apatite crystals within metamorphic and auriferous quartz veins can be grouped into three generations according to cathodoluminescence imaging and trace element concentrations: Ap1 precipitated in the pre-mineralization metamorphic stage, whereas Ap2 and Ap3 formed in the auriferous hydrothermal stage. Metamorphic Ap1 displays a negative Eu anomaly, indicating a predominance of Eu^{2+} and crystallization under relatively reduced conditions. On the other hand, syn-gold hydrothermal Ap2 and Ap3 have marked positive Eu anomalies. Radiometric ages for metamorphic Ap1 are at ca. 461 Ma, whereas hydrothermal Ap2 and xenotime from auriferous quartz gave U-Pb ages of 425 ± 15 Ma and 416 ± 15 Ma, interpreted as the time of gold mineralization. Emplacement ages determined by U-Pb zircon data are 439 ± 2 Ma for granitic intrusion and 427 ± 2 Ma for a mafic dike in the mining district. Mineralization, therefore, postdates the metamorphism of local host rocks and granitic magmatism by ~35 ± 24 m.y. and ~14 ± 17 m.y., respectively. The synchronism of gold genesis and mafic magmatism provides additional evidence for a mantle derivation of the ore-forming fluids. The highly radiogenic $^{87}Sr/^{86}Sr$ ratios obtained for Ap1 (0.7178–0.7302) are consistent with its precipitation from a metamorphic fluid. Higher Sr concentrations (Ap2 = 1228–2884 ppm, Ap3 = 2325–3169 ppm) and positive Eu anomalies (Eu/Eu*: Ap2 = 1.03–2.84, Ap3 = 2.00–4.30) but lower and variable $^{87}Sr/^{86}Sr$ ratios in hydrothermal Ap2 (0.7100–0.7165) and Ap3 (0.7086–0.7116) are mainly ascribed to extensive fluid-wall rock exchange of Sr during mineralization. It is therefore suggested that fluid-rock reaction played a vital role in the observed positive Eu anomalies of hydrothermal apatite. Our study highlights the usefulness of apatite as a novel and robust geochronological, geochemical, and isotopic indicator of complex mineralization processes in hydrothermal gold deposits.

1. INTRODUCTION

Apatite is a ubiquitous accessory mineral in diverse rock types and hydrothermal ores and has a unique crystal structure that can accommodate a wide range of trace elements (Pan and Fleet, 2002; Mao et al., 2016). It occurs in a variety of hydrothermal and magmatic ore deposits, including orogenic Au deposits (Robert and Brown, 1986; Bloem et al., 1994; Brugger et al., 2000; Williams, 2007; Hazarika et al., 2016; Zheng et al., 2022) and other Au deposit types (Barker et al., 2009; Bath et al., 2013; Ma et al., 2022a), volcanogenic massive sulfides (Genna et al., 2014), U unconformity-type (Gaboreau et al., 2007), porphyry Cu-Au-Mo (Cao et al., 2021; Qu et al., 2022), granite-related W-Sn (Zhang et al., 2021), iron oxide copper-gold (IOCG) (Krneta et al., 2016), iron oxide apatite (Harlov et al., 2002a), pegmatite (Cao et al., 2013), carbonatite-related rare earth element (Ying et al., 2020), magmatic Ni-Cu-platinum group element deposits (Liu et al., 2021), and diamondiferous kimberlite (Malarkey et al., 2010).

The geochemical composition of apatite has been used to constrain the features and genesis of igneous (Chu et al., 2009) and metamorphic (Kusebauch et al., 2015) rocks and as a tracer of the mineralization process (Palma et al., 2019; Zeng et al., 2016). Apatite reacts sensitively to changing hydrothermal conditions via coupled dissolution-reprecipitation (CDR) reactions in aqueous metasomatic systems (Harlov and Förster, 2003). Therefore, newly formed replacement apatite is assumed to be in local equilibrium with hydrothermal fluid and should reflect the composition of the fluid (Harlov et al., 2002b; Jones et al., 2014). As such, the trace element chemistry of apatite may reveal changes in the pH, oxidation state, temperature, and origin of the ore-forming fluids (Andersson et al., 2019; Palma et al., 2019; Ma et al., 2022a; Qu et al., 2022). Apatite has been utilized to unravel various hydrothermal processes, especially the magmatic fluid evolution and associated mineralization. Recent research on apatite has covered diverse types of ore deposits. Mao et al. (2016) discriminated apatite from various genetic types of ore deposits, including orogenic Ni-Cu, epithermal and orogenic Au, IOCG, Kiruna, porphyry, skarn, and carbonatite rare earth element (REE) deposits, and various ore-barren mafic to felsic rocks and subdivided them into different groups to make apatite a reliable proxy for mineral exploration. Qu et al. (2022) demonstrated

Shao-Yong Jiang https://orcid.org/0000-0003-3921-739X

†Corresponding author: shyjiang@cug.edu.cn.

GSA Bulletin;
published online 10 March 2023

https://doi.org/10.1130/B36642.1; 16 figures; 1 supplemental file.

that apatite's textural and geochemical features could record the magmatic-hydrothermal evolution of porphyry systems.

Apatite strontium isotope compositions have been utilized to trace fluid sources, pathways, ore genesis, and fluid evolution in many magmatic-hydrothermal deposits (Chen et al., 2014; Zhao et al., 2015; Kozlik et al., 2016; Li et al., 2022a). In the Rb-Sr isotope system, ^{87}Rb undergoes negative beta decay to ^{87}Sr through the equation $^{87}Rb = {}^{87}Sr + \beta^- + \nu + Q$, where β^- is the beta particle, ν is an antineutrino, and Q is the decay energy. As a calc-phosphate and essentially free of potassium, apatite contains negligible Rb and high abundances of Sr, with a very low Rb/Sr ratio (Creaser and Gray, 1992). As such, the present-day apatite Sr isotopes preserve the fluid isotope composition at the time of deposition (Li et al., 2022b). Despite the successful application of apatite chemistry and Sr isotope ratios in interpreting ore-forming processes and fluid sources in magmatic-hydrothermal deposits, it has not received much attention in genetic investigations of mineral deposits that formed in metamorphic settings. Furthermore, apatite is highly resistant to weathering and post-mineralization modifications. Its low to high lattice-bound concentrations and high blocking temperatures for Pb diffusion (~550 °C; Kirkland et al., 2018) make it well suited for dating mineral deposits (e.g., Chen et al., 2019; Glorie et al., 2019; Fox et al., 2021; Li et al., 2022a; Ma et al., 2022b).

From an economic perspective, orogenic gold deposits are among the most important Au deposits worldwide and characteristically occur as poly-stage disseminations or quartz-sulfide veins within expansive panels of mineralized, deformed, and metamorphosed volcano-sedimentary sequences (Groves, 1993; Goldfarb et al., 2005; Frimmel, 2018). However, accurate dating of this family of gold deposits is challenging due to the absence of suitable chronometers. The absence of precise ages has hampered our understanding of the interplay between Au mineralization and volcanism, plutonism, sedimentation, metamorphism, and deformation, leading to the ongoing debate on the source of the ore fluids, as well as that of the metals transported by them. The following hypotheses are currently under discussion for the fluid source in orogenic Au deposits: (1) locally sourced from metamorphic devolatilization reactions of volcano-sedimentary rocks (Large et al., 2009; Thomas et al., 2011); and (2) deeply sourced reservoirs, including magmatic (Xue et al., 2013), mantle (Groves et al., 2019), and metamorphic fluids (Pitcairn et al., 2006; Tomkins, 2010). In addition, orogenic gold deposits are generally products of complicated polyphase hydrothermal systems that invoked multiple fluids at different times during their formation and deformation history, as indicated by the presence of multiple generations of veins, texturally complex gangue and ore minerals, and various types of fluid inclusions (Shelton et al., 2004; Taylor et al., 2021). This makes it challenging to clearly decipher multiple fluid overprints involved in the hydrothermal system and evaluate the role of different fluids in gold mineralization. Furthermore, post-mineralization hydrothermal superpositions may partially or totally reset the isotopic characteristics of the dated minerals, causing further difficulties in accurately constraining the age of ore formation.

The South China Block (SCB) hosts currently the third largest gold province in China, with a total Au resource of over 1000 t (Deng and Wang, 2016; Xu et al., 2017). Lode gold deposits in the SCB mainly occur within the low- to high-grade metamorphosed Neoproterozoic volcano-sedimentary sequences (Xu et al., 2017; Zhang et al., 2019). Previous geochronological data reveal that the Neoproterozoic, early Paleozoic, and early Mesozoic periods were fertile for lode gold mineralization in the SCB (Ni et al., 2015; Zhang et al., 2019). These deposits have been studied for decades, but there is no consensus on their sources of ore fluids and metals or mineralization processes (e.g., Goldfarb et al., 2019; Zhang et al., 2019). Two principal genetic models prevail: orogenic (Ni et al., 2015; Goldfarb et al., 2019; Zhang et al., 2019) and intrusion-related (Peng and Frei, 2004; Li et al., 2018a, 2018b, 2021a). Uncertainty regarding the ore genesis of lode gold deposits in the SCB is primarily due to the lack of solid constraints on the timing of mineralization and a poor understanding of the detailed ore-forming processes.

The large Shuangqishan Au deposit (gold resources >20 t), situated within an orogenic terrane with polyphase evolution in South China, represents an exceptional case of such a system that is highly complex due to the presence of multiple local and regional hydrothermal events that might be related or unrelated to Au mineralization (Li, 2010; Ma et al., 2021). Many methods have been attempted to date the mineralization in this deposit, including the Rb-Sr and U-Th-Pb dating of hydrothermal minerals (e.g., quartz, chlorite, pyrite, and apatite). They yielded highly variable ages ranging from Paleozoic to late Mesozoic (Huang, 2001; Wu, 2002; Bao et al., 2020; Ma et al., 2021). The controversy over the absolute timing of Au mineralization is reflected by divergent ideas on the ore genesis: (1) the researchers who favor a broadly 440 Ma age for Au mineralization hold the view that auriferous fluids were derived from metamorphic dewatering of supracrustal volcano-sedimentary rocks or subcrustal fertilized mantle lithosphere-derived origins (Kou et al., 2016; Ma et al., 2021); (2) in contrast, those who ascribe a Late Jurassic (ca. 160 Ma) age to the mineralization explain it by granite-derived magmatogenic hydrothermal fluids (Bao et al., 2020).

Despite the successful application of U-Pb geochronology, mineral chemistry, and Sr isotope analyses to apatite in reconstructing ore-forming processes and establishing genetic models in various mineral deposits, it has not received much attention in genetic studies of orogenic gold deposits. Here we document the complex textural relationships and geochemistry of apatite from metamorphic and gold-mineralized quartz veins at Shuangqishan. We first define the origin of the apatite; secondly, we use laser ablation–inductively coupled plasma–mass spectrometry (LA-ICP-MS) U-Pb dating of apatite and zircon from host rocks, igneous rocks, and gold ores, together with sensitive high-resolution ion microprobe (SHRIMP) U-Pb dating of gold-related hydrothermal xenotime to establish the timing of metamorphism, magmatism, and lode gold mineralization; thirdly, we utilize the textural, trace element, and Sr isotopic compositions of apatite to discriminate between regional metamorphism and hydrothermal gold mineralization, and then assess the likely origin of the multistage hydrothermal fluids involved in the formation of the Shuangqishan deposit. This case study demonstrates the usefulness of apatite as a tracer of ore-forming fluid evolution and provides valuable constraints on the source of orogenic gold deposits.

2. GEOLOGICAL SETTING AND AU MINERALIZATION

The Shuangqishan gold deposit is located in the center of the Dehua goldfield in the southeastern coastal area of South China (Figs. 1A and 1B). During the Jinningian Orogeny (900–820 Ma), the Yangtze and Cathaysia blocks were accreted along the Jiangshao suture zone and formed the Jiangnan Orogen (Zhao et al., 2011). Crustal-scale rifting prevailed during the late Neoproterozoic to early Paleozoic (820–460 Ma) evolution of South China, leading to the Nanhua

Figure 1. (A) Simplified tectonic units of China. (B) Schematic map showing the distribution of major orogenic gold deposits in the South China Block (after Goldfarb et al., 2019; Ma et al., 2021). (C) The simplified geologic map of the Dehua goldfield shows the distribution of regional structures, strata, granites, and major gold deposits (modified after Li, 2010). JSF—Jiangshan-Shaoxing Fault.

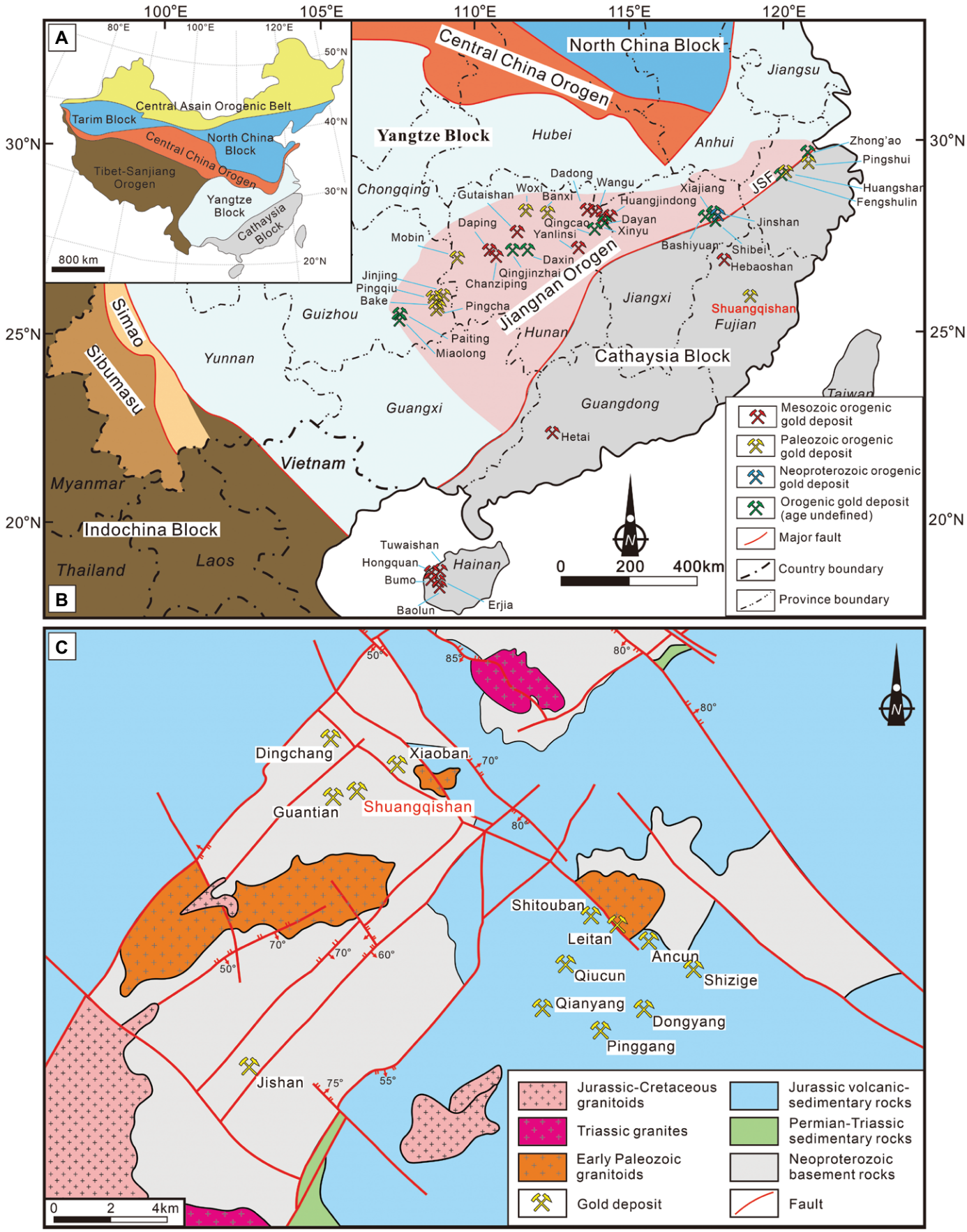

Rift and generating abundant continental to neritic marine sedimentary and bimodal volcanic rocks (Wang and Li, 2003). After that, South China experienced poly-stage crustal reworking during Caledonian, Indosinian, and Yanshanian tectono-thermal events. The Caledonian Orogeny, also termed the Wuyi-Yunkai Orogeny (Li et al., 2010), inverted the Nanhua Rift and resulted in crustal thickening, nappe structures, and high-grade metamorphism (Faure et al., 2009; Charvet et al., 2010). Peak metamorphism, reaching amphibolite facies, took place between ca. 460 and 440 Ma (Li et al., 2010), followed by orogenic collapse at ca. 440–390 Ma, accompanied by exhumation, extension, and partial melting (Li et al., 2010). The Indosinian Orogeny (240–210 Ma) is marked by a Late Triassic unconformity, Early-Middle Triassic ductile shearing, folding, metamorphism, and plutonism (Li and Li, 2007). Since the Jurassic, South China has been dominated by Pacific tectonism, i.e., by the oblique subduction of the paleo-Pacific oceanic lithosphere underneath the southeastern margin of the Eurasian plate (Zhou et al., 2006). This Yanshanian tectonic event produced the Jurassic to Cretaceous granitoid-volcanic belt in southeastern China (Zhou et al., 2006).

As a result, the Precambrian metamorphic basement, late Paleozoic-Middle Jurassic sedimentary rocks, and Jurassic volcano-sedimentary sequences make up the major lithostratigraphic units of the Dehua goldfield (Fig. 1C). The dominant granitoids in the Dehua area comprise early Paleozoic, Triassic, and Jurassic-Cretaceous intrusions (Fig. 1C). Many mafic dikes have also been identified in this region (Ma et al., 2021).

Shuangqishan represents a complex, shear zone-hosted, veined gold minerals system within Neoproterozoic volcano-sedimentary rocks of the Daling Formation that metamorphosed at greenschist- to amphibolite-facies conditions (Fig. 2). A detailed characterization of Shuangqishan's local geology, mineralization style, and paragenetic sequence is provided by Ma et al. (2021, 2022c) and only summarized here. The Shuangqishan deposit consists of a series of discontinuous Au orebodies which are confined to highly strained rocks related to 2- to 10-m-wide NW- and NE-striking brittle-ductile shear zones developed in the volcano-sedimentary sequences of the Daling Formation (Fig. 2). Intrusive rocks, including Silurian quartz monzodiorite and diorite, and Jurassic to Cretaceous mafic-felsic dikes composed of diabase, diorite, quartz porphyry, and granite porphyry, were emplaced within the Daling Formation (Fig. 2).

The Shuangqishan deposit was discovered in 1986 and has been mined since 1995. Twenty-two auriferous quartz veins have been identified in the mica schist and interlayered mafic-felsic metavolcanic rocks. These veins extend vertically up to 420 m, and their lengths and widths vary from 80 to 560 m and from 0.8 to 2.9 m, respectively. Reserves of over 20 t Au with an average grade of 9 g/t have been identified at Shuangqishan (Li, 2010). The so-called 13Au is the largest orebody (reserves ~7.5 t Au), extending from 578 to 487 m in elevation, dipping to northeast at 26–39°.

The Shuangqishan ore is sulfidic and occurs as veinlets and stockwork of pervasive quartz ± calcite veins, and it can be broadly divided into three stages (Fig. 3): Stage I is represented by the syn-metamorphic deposition of coarse-grained, milky white quartz veins. These veins display brittle-ductile deformation structures and textures (Fig. 4A; Ma et al., 2021). The syn-mineralization Stage II involved the overprinting of the barren quartz veins by later gray auriferous sulfide-quartz veins (Figs. 4B–4D), and can be separated into two sub-stages based on their distinct mineral assemblages: Sub-

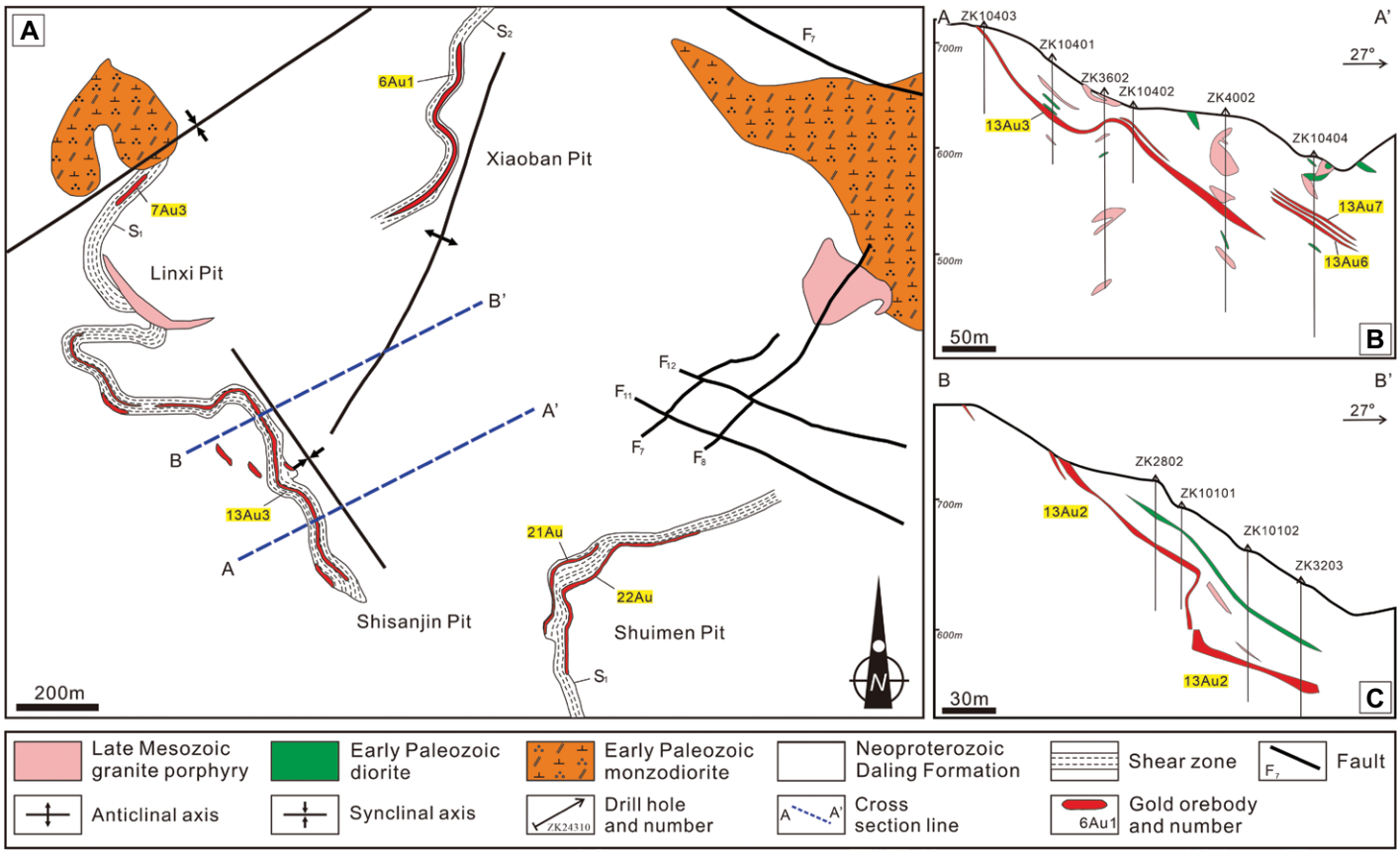

Figure 2. (A) Geological sketch map of the Shuangqishan Au deposit of southeastern China. (B and C) Simplified geologic cross-sections from the Shuangqishan Au deposit show the distribution of orebodies (after Li, 2010).

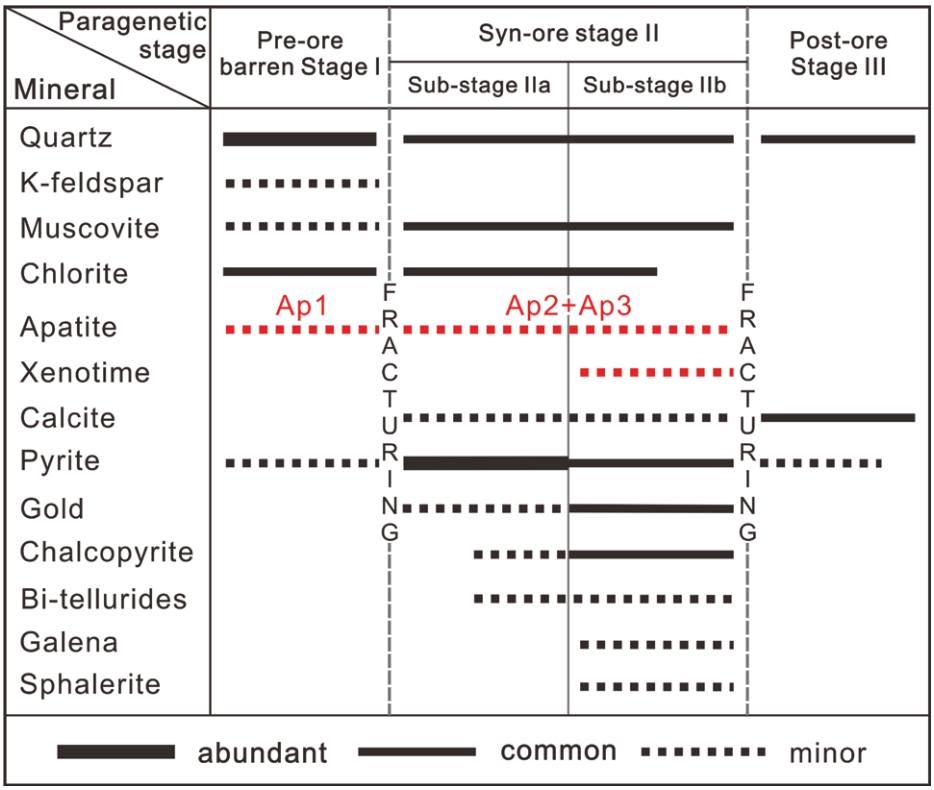

Figure 3. Wall-rock and vein paragenetic mineral sequences for the Shuangqishan gold deposit of southeastern China (modified after Ma et al., 2021).

stage IIa is more volumetrically important and mainly contains pyrite with minor native gold (Fig. 4E); Sub-stage IIb is more Cu- and Au-rich and is dominated by chalcopyrite and pyrite with gold and Bi-Te minerals typically occurring as μm-wide veins filling the fractures of pyrite and chalcopyrite (Fig. 4F). Late quartz-calcite veins define the Au-deficient Stage III. Hydrothermal alteration accompanying mineralization is extensive in wall rock proximal to the auriferous quartz veins. The alteration assemblages consist mainly of sericite, chlorite, quartz, calcite, apatite, xenotime (Figs. 5 and 6), and minor disseminations of pyrite with no clear zonation.

3. ANALYTICAL METHODS

Representative samples of metamorphic quartz veins and auriferous quartz-sulfide veins in surrounding mineralized and altered metamorphic rocks were collected from underground tunnels at the 512-m and 562-m levels. Polished sections of metamorphic (barren) and mineralized quartz veins that contain apatite grains were observed under scanning electron microscope (SEM) and OP-CL to characterize the structures of these minerals. Zircon was carefully separated from two metamorphic rock samples (19SQS-12 and 19SQS-13). Zircon grains from a quartz monzodiorite sample (16SQS23-2) and a diorite dike (16SQS1-3) were also selected for U-Pb dating. Additionally, 3- to 5-mm-diameter round chips containing xenotime crystals were drilled from thin sections of a high-grade quartz sulfide vein sample (16SQS22-2) and mounted in epoxy. The analytical methods are summarized below, and more standard and specific details are given in Supplementary Material 1.[1]

[1]Supplemental Material. Text: Analytical methods and analytical data. Table S1: LA-ICP-MS zircon U-Th-Pb isotope data of ore-hosting metamorphic rocks of the Shuangqishan gold deposit. Table S2: LA-ICP-MS U-Th-Pb isotope data for zircon grains from the diorite and granite porphyry dikes in the Shuangqishan gold deposit. Table S3: LA-ICP-MS apatite (Ap1 and Ap2) U-Th-Pb data of metamorphic and auriferous quartz veins from the Shuangqishan gold deposit. Table S4: Trace-element concentrations in multiple-generation apatite from the Shuangqishan gold deposit, analyzed by LA-ICP-MS. Table S5: In-situ Sr isotopic compositions of multiple-generation apatite from the Shuangqishan gold deposit, analyzed by LA-MC-ICP-MS. Table S6: Electron microprobe geochemical data for hydrothermal xenotime from the Shuangqishan gold deposit. Table S7: SHRIMP U-Th-Pb isotope data for hydrothermal xenotime from the sub-stage IIb gold ores in the Shuangqishan gold deposit. Please visit https://doi.org/10.1130/GSAB.S.21597816 to access the supplemental material, and contact editing@geosociety.org with any questions.

Optical cold CL photomicrography was performed on polished thin sections containing apatite grains using an Olympus microscope attached to a RELIOTRON III CL stage housed at the State Key Laboratory of Geological Processes and Mineral Resources, China University of Geosciences, Wuhan (GPMR-CUG). In addition, backscattered electron (BSE) imaging was utilized to characterize the morphological and textural features of apatite and xenotime in each sample using a JEOL JCM-7000 environmental SEM housed at the Collaborative Innovation Center for Exploration of Strategic Mineral Resources, CUG.

In situ zircon and apatite U-Pb dating and trace element analyses of apatite were performed by LA-ICP-MS housed at the GPMR-CUG, using an ArF excimer laser system (GeoLas Pro, 193-nm wavelength) and a quadrupole ICP-MS (Thermo iCap). Xenotime grains of sufficient size (>20 μm in diameter) were drilled out from the polished thin sections of auriferous pyrite-rich vein material into ~2 mm plugs and then cast into a 25 mm epoxy mount along with standards. The mount was analyzed using the SHRIMP-II housed at the Research School of Earth Sciences, Australian National University (Canberra, Australia). In situ Sr isotope analysis of apatite spots was obtained by the same laser ablation system coupled to a Nu Plasma multi-collector (MC)-ICP-MS housed at GPMR-CUG.

4. RESULTS

4.1. U-Pb Age of Zircon

Four samples, comprising amphibolite (sample 19SQS-13) and biotite gneiss (sample 19SQS-12) from ore-hosting metamorphic rocks, a quartz monzodiorite sample (16SQS23-2), and a diorite dike (16SQS1-3), were selected for U-Pb zircon dating. All analyzed zircon grains are transparent euhedral crystals up to 200 μm in size (Fig. 7). They are characterized by oscillatory zonation under CL (Fig. 7), indicating a magmatic origin (Corfu et al., 2003). Fifteen analyses of zircon grains in amphibolite yielded 220–1765 ppm Th and 145–1170 ppm U with high Th/U ratios (0.7–2.7) (Table S1). All the analyzed zircon grains in amphibolite are concordant (Fig. 7A) and yield a weighted mean $^{206}Pb/^{238}U$ age of 762.0 ± 11.0 Ma (1σ, n = 15, mean square weighted deviation [MSWD] = 4.1). Twenty spot analyses of 20 zircon grains in biotite gneiss yielded Th and U concentrations of 77–693 ppm and 49–282 ppm, respectively, and high Th/U ratios (1.4–2.7). Their weighted mean $^{206}Pb/^{238}U$ age is 734.8 ± 5.2 Ma (1σ, n = 20, MSWD = 0.64) (Fig. 7B). Twenty three analyses on zircon

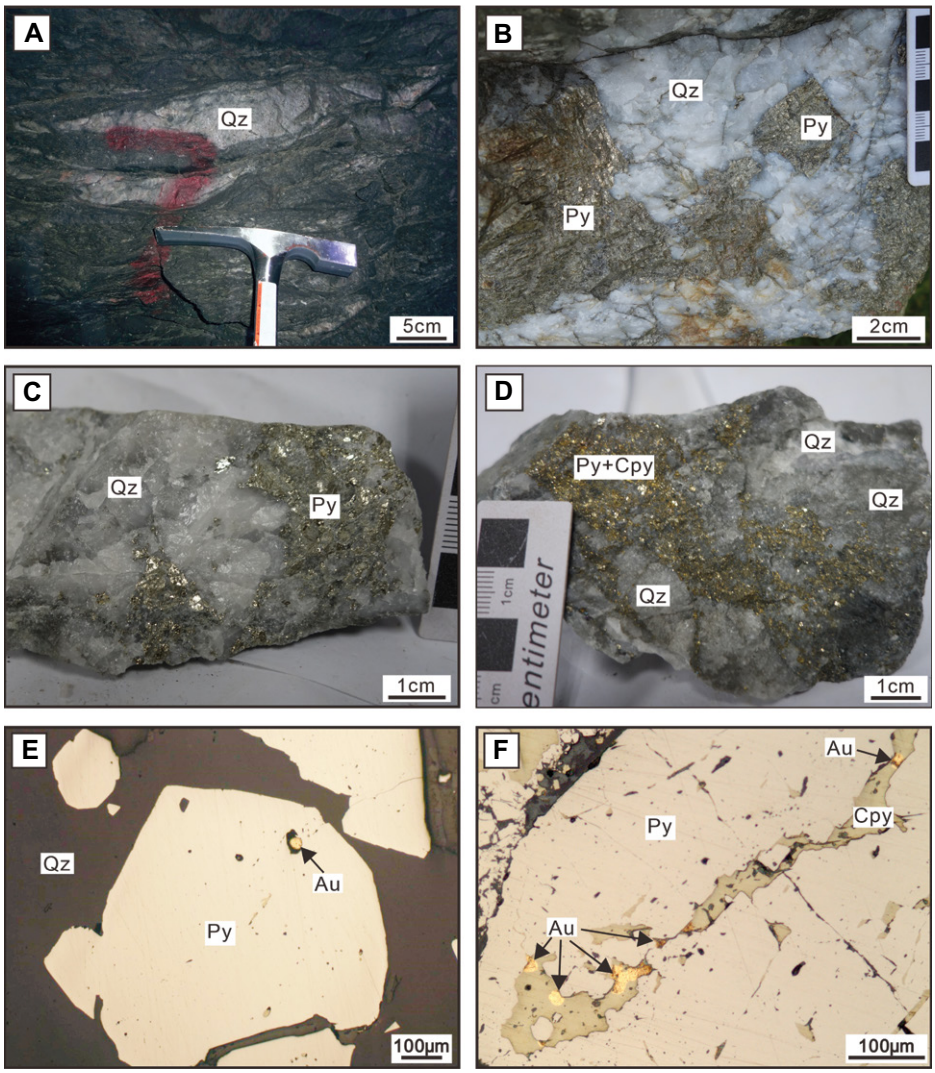

Figure 4. Photographs (A–D) and reflected-light photomicrographs (E and F) showing the mode of gold ore textures at Shuangqishan in southeastern China. (A) Underground stope ceiling displaying pinch-and-swell structures in ore-barren metamorphic quartz veins. (B) Large crystals of pyrite dispersed in a milky quartz vein. (C) Smoky quartz and pyrite in barren white quartz veins. (D) Gray-colored quartz-pyrite-chalcopyrite veins. (E) Rounded native gold inclusions within pyrite. (F) Gold-chalcopyrite veins filling fractures in pyrite. Au—native gold; Cpy—chalcopyrite; Py—pyrite; Qz—quartz.

grains from sample 16SQS23-2 returned concordant ages with a mean $^{206}Pb/^{238}U$ age of 438.9 ± 2.0 Ma (1σ, MSWD = 0.1) (Table S2; Fig. 8A). The zircon grains from sample 16SQS1-3 gave $^{206}Pb/^{238}U$ ages between 448.1 ± 8.6 Ma and 414.3 ± 11.4 Ma with a weighted mean of 426.5 ± 1.8 Ma (Fig. 8B).

4.2. Apatite

Examination of crosscutting and replacement relationships and textural characteristics allowed the identification of three generations of apatite at Shuangqishan: Ap1 can be found in Stage I metamorphic quartz veins and Stage II gold-bearing quartz-sulfide veins; Ap2 and Ap3 are recognized in both of sub-stage IIa quartz-pyrite and sub-stage IIb quartz-chalcopyrite-pyrite veins. All three generations of apatite are recognized within the quartz veins in the underground tunnels at the 512-m and 562-m levels and show no evident spatial distribution characteristics. Ap1 is commonly associated with quartz, chlorite, and muscovite within Stage I metamorphic quartz veins. Ap1 is locally aligned or elongated along with the foliation of the host rocks. It is euhedral to subhedral, inclusion-free, and transparent, with grain size ranging mainly from 50 to 300 μm. It commonly displays a uniform bright green luminescence in the optical cathodoluminescence (OP-CL) image (Fig. 5A). Apatite from Stage II auriferous quartz-sulfide veins generally consists of two generations as revealed by BSE and OP-CL images: a fractured and porous core (Ap1) with bright green luminescence (Figs. 5B and 5C), followed by a pore-free overgrowth (Ap2) with dark green luminescence (Figs. 5B and 5C). Ap2 is anhedral and occurs as slim overgrowths (~10–100 μm) or, in places, as medium-sized to large (100–2000 μm) individual grains that show a close spatial association with auriferous pyrite (Fig. 5D). In some sub-stage IIb gold-rich ores, apatite displays a complex core-mantle-rim texture, with an Ap1 core, an Ap2 mantle, and an Ap3 rim with blue luminescence (Fig. 5E).

The U-Pb data of Ap1 and Ap2 are listed in Table S3. The Tera-Wasserburg diagrams of apatite and xenotime are shown in Figures 9 and 10, respectively. Forty-one analyses on Ap1 from Stage I metamorphic quartz veins define a lower intercept age of 460.5 ± 9.3 Ma (2σ, MSWD = 2.5) with an initial $^{207}Pb/^{206}Pb$ of 0.916 ± 0.009 (Fig. 9A). The weighted average $^{206}Pb/^{238}U$ age after ^{207}Pb-correction is 459.3 ± 6.3 Ma (2σ, MSWD = 2.6), consistent with its lower intercept age (Fig. 9A). On the Tera-Wasserburg diagram (Fig. 9B), the 20 analyses on Ap2 from Stage II auriferous quartz-sulfide veins define a regression line with a lower intercept at 425.0 ± 15.0 Ma (2σ, MSWD = 1.1) with initial $^{207}Pb/^{206}Pb$ of 0.866 ± 0.009. The common-Pb corrected $^{206}Pb/^{238}U$ age yielded a weighted mean age of 423.0 ± 7.2 Ma (2σ, MSWD = 2.9). Additionally, we have rechecked the apatite spots analyzed by Ma et al. (2021) and found that some of the spots were performed on the metamorphic cores of the apatite in that sample. When excluding those metamorphic domains (dashed blue ellipses in Fig. 9C), the remaining hydrothermal rims define a younger regression line with a lower intercept age of 422.0 ± 12.0 Ma (2σ, MSWD = 1.1) than that reported by Ma et al. (2021) (436.8 ± 7.6 Ma). This recalculated age is within error consistent with the new U-Pb age of Ap2 presented in this paper. Due to their low U but high common Pb concentrations, no meaningful U-Pb dates were generated from Ap3 grains.

The trace element contents of the three apatite generations analyzed by LA-ICP-MS are summarized in Table S4. Box charts indicate that the abundances of some trace elements are variable among different apatite generations (e.g., Mn, Ga, Ge, As, Sr, Y, and REE; Fig. 11). The Ap1 crystals in metamorphic and auriferous quartz veins share very similar concentrations of many

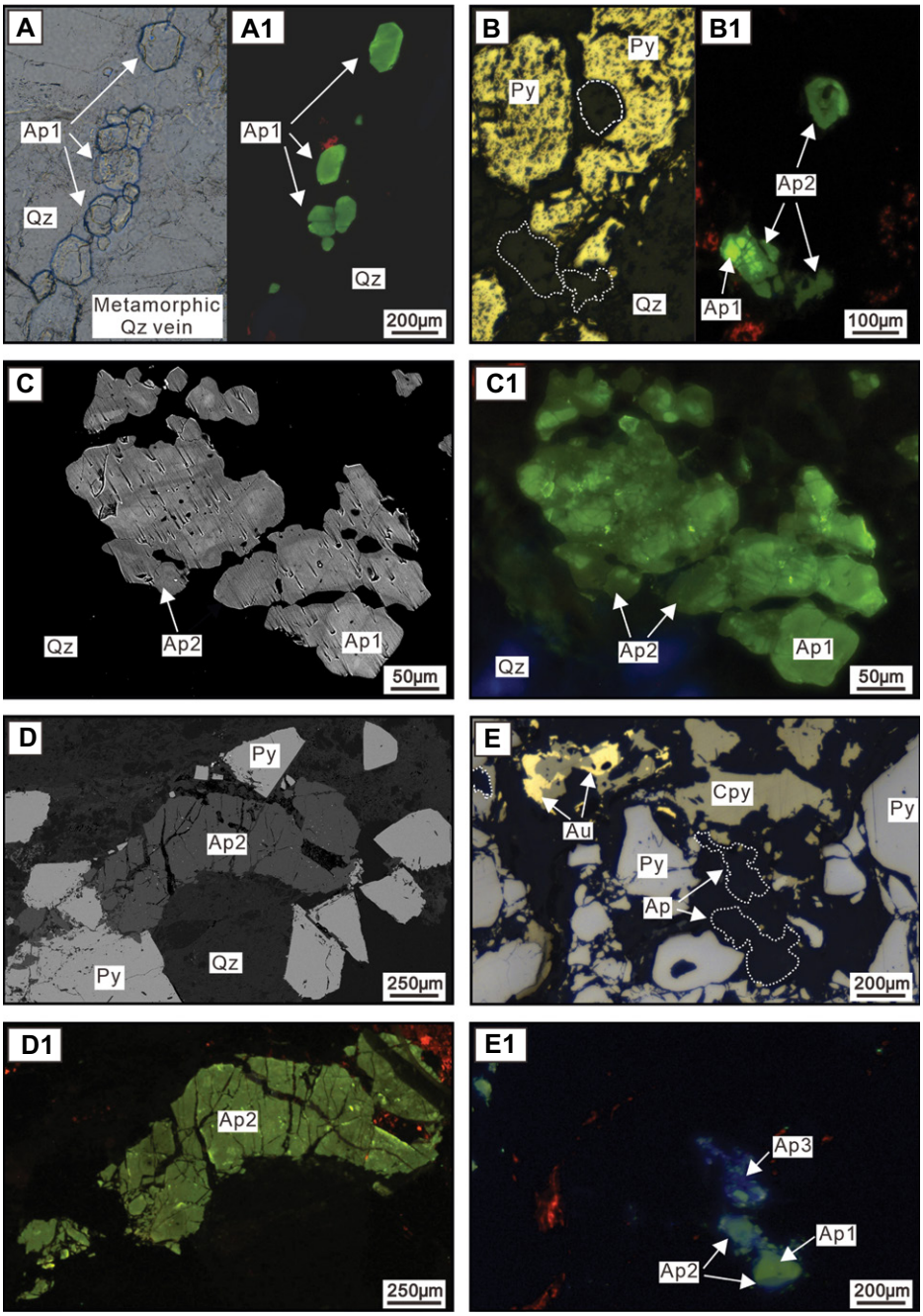

Figure 5. Transmitted (A), reflected (B and E), back-scattered electron (C and D), and microscopic cathodoluminescence (A1–E1) photomicrographs of representative apatite grains from metamorphic barren and gold-mineralized quartz veins in the Shuangqishan gold deposit of southeastern China. (A) Idiomorphic Ap1 grains within metamorphic quartz veins. (B) Apatite crystals enclosed in auriferous pyrite, one apatite grain shows a core-rim texture with an Ap2 overgrowth on Ap1. (C) Ap1 + Ap2 aggregates within auriferous quartz veins. (D) A brecciated Ap2 grain is intergrown with gold-bearing pyrite. (E) One apatite grain with a core (Ap1)-mantle (Ap2)-rim (Ap3) texture coexisting with native gold, chalcopyrite, and pyrite. Ap—apatite; Au—native gold; Cpy—chalcopyrite; Py—pyrite; Qz—quartz.

elements, and they are enriched in Mn, As, Y, REE, and U compared to Ap2 and Ap3. However, Ap1 in the metamorphic veins is slightly depleted in Ga, Ge, and Pb compared to those in the gold-mineralized quartz veins. In the auriferous quartz veins, the abundances of Mn, Ga, Ge, As, Y, and REE in apatite show an apparent decrease trend from Ap1 to Ap3 (Fig. 11).

Chondrite-normalized REE patterns show that Ap1 from metamorphic and Au-mineralized quartz veins is strongly enriched in the middle (M)REE (Sm to Dy) and depleted in the light (L)REE and high (H)REE (Figs. 12A and 12B). All REE patterns of Ap1 display a distinct negative Eu anomaly (Figs. 12A and 12B; Eu/Eu* = 0.38–0.95) and a slight positive Ce anomaly (Ce/Ce* = 1.03–1.20). Ap2 and Ap3 crystals have similar REE patterns, i.e., enriched in MREE, relatively enriched in the LREE, and strongly depleted in HREE (Figs. 12C and 12D). Ap3 (Eu/Eu* = 2.00–4.30) displays a more evident negative Eu anomaly compared to Ap2 (Eu/Eu* = 1.03–2.84) (Fig. 13).

The $^{87}Sr/^{86}Sr$ ratios measured on apatite from different vein stages are summarized in Table S5. Ap1 from ore-barren metamorphic quartz veins has a wide range of $^{87}Sr/^{86}Sr$ ratios (0.7223–0.7302, mean = 0.7255). In auriferous quartz veins, fine-grained Ap2 rims have significantly lower $^{87}Sr/^{86}Sr$ ratios (0.7100–0.7165, mean = 0.7135) than those in the cores of medium-grained Ap1 (0.7178–0.7271, mean = 0.7230). Ap3 in the Au-mineralized quartz veins has consistently lower $^{87}Sr/^{86}Sr$ ratios of 0.7086–0.7116 (mean = 0. 7096).

4.3. Xenotime Occurrences and U-Pb Age

The mineralized samples from substage IIb quartz-chalcopyrite-pyrite ores contain accessory anhedral or irregular-shaped xenotime grains that are 5–40 μm in size (Fig. 6). In many places, the xenotime crystals grew on the edge of, or in contact with, deformed pyrite (Fig. 6A) or chalcopyrite (Fig. 6B). Major element concentrations and in situ SHRIMP U-Th-Pb results of xenotime are provided in Tables S6 and S7. Eleven analyses were conducted on 11 larger grains with homogeneous surfaces and no inclusions. On the Tera-Wasserburg diagram, the 11 spots define a regression line (Fig. 10) that yielded a lower intercept age of 416.0 ± 15.0 Ma (1σ, MSWD = 0.88) and an upper intercept of $^{207}Pb/^{206}Pb = 0.903 \pm 0.066$.

5. DISCUSSION

5.1. Apatite as a Monitor of Metamorphic and Hydrothermal Fluids

5.1.1. Origin of the Multiple-Generation Apatite

The complex textures and chemical compositions recorded by polystage apatite grains at Shuangqishan make it possible to infer their origin. Ap1 from Stage I gold-barren metamorphic quartz veins is of metamorphic

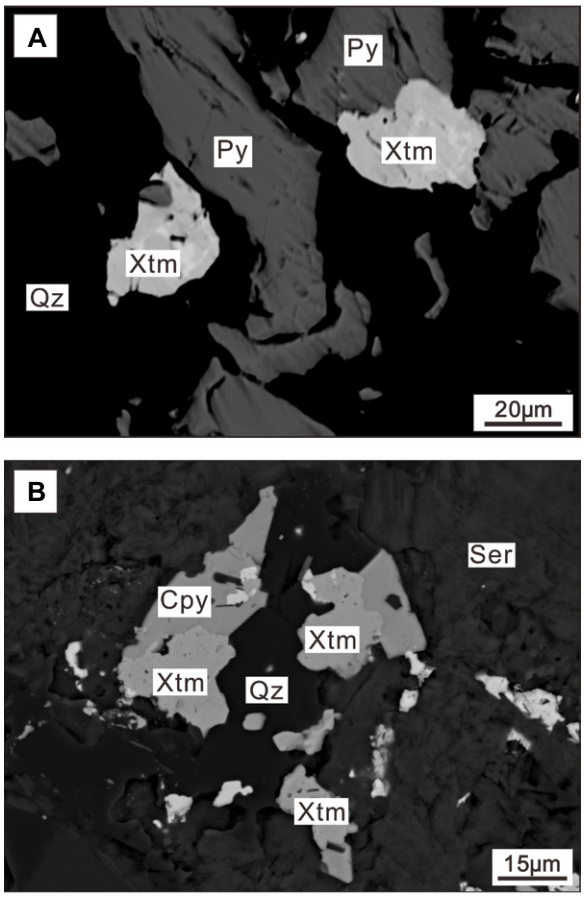

Figure 6. Back-scattered electron images of hydrothermal xenotime crystals within Assemblage II quartz-pyrite-chalcopyrite veins of the Shuangqishan deposit of southeastern China. (A) Hydrothermal xenotime grains coexist with deformed pyrite grains. (B) Xenotime crystals coexist with chalcopyrite. Cpy—chalcopyrite; Py—pyrite; Qz—quartz, Ser—sericite; Xtm—xenotime.

origin. Texturally, this apatite generation is euhedral in shape and aligned along the foliation of the host rocks (Fig. 5A). The analyzed Ap1 shows no evidence of hydrothermal alteration (Fig. 5A) and has the highest REE + Y and Mn abundances (Fig. 11). It is enriched in MREE and displays distinct negative Eu anomalies (Fig. 12A), features characteristic of metamorphic apatite elsewhere (Henrichs et al., 2018).

In contrast, the apatite in the mineralized quartz veins displays a distinct core-(mantle)-rim texture in OP-CL images, with a bright green core (Ap1) overgrown by a dark green rim (Ap2); locally, blue-colored Ap3 occurs as overgrowths of Ap1 and Ap2 (Fig. 5). Ap1 crystals in the auriferous quartz veins share many features (e.g., textures and REE patterns; Figs. 11 and 12) identical to those in metamorphic quartz veins and are interpreted to be metamorphic in origin. Under BSE imaging, the Ap1 crystals within Stage II auriferous quartz veins commonly show textures of fluid metasomatism (Fig. 5C). These altered Ap1 domains are characterized by pitted surfaces with visible voids (Fig. 5C). These features are consistent with a fluid-aided, coupled dissolution-reprecipitation (CDR) process (Putnis, 2002). As a result of metasomatism, there could be complex chemical exchanges between the Ap1 and the later auriferous hydrothermal fluids. During the CDR process, some elements (Sr and Pb) have been leached out of the Ap1 within Stage II veins and show a pronounced depletion compared to those in Ap1 within metamorphic quartz veins (e.g., Harlov et al., 2003). On the other hand, the reactive hydrothermal fluids may be enriched in some other elements (e.g., Ga, Ge, and Th) and lead to higher Ga, Ge, and Th concentrations in the metasomatic Ap1 within Stage II veins. The intimate textural relationships with native gold, sulfides, and other ore-stage hydrothermal alteration phases (Figs. 5B–5E) indicate that the Ap2 and Ap3 grains are hydrothermal in origin

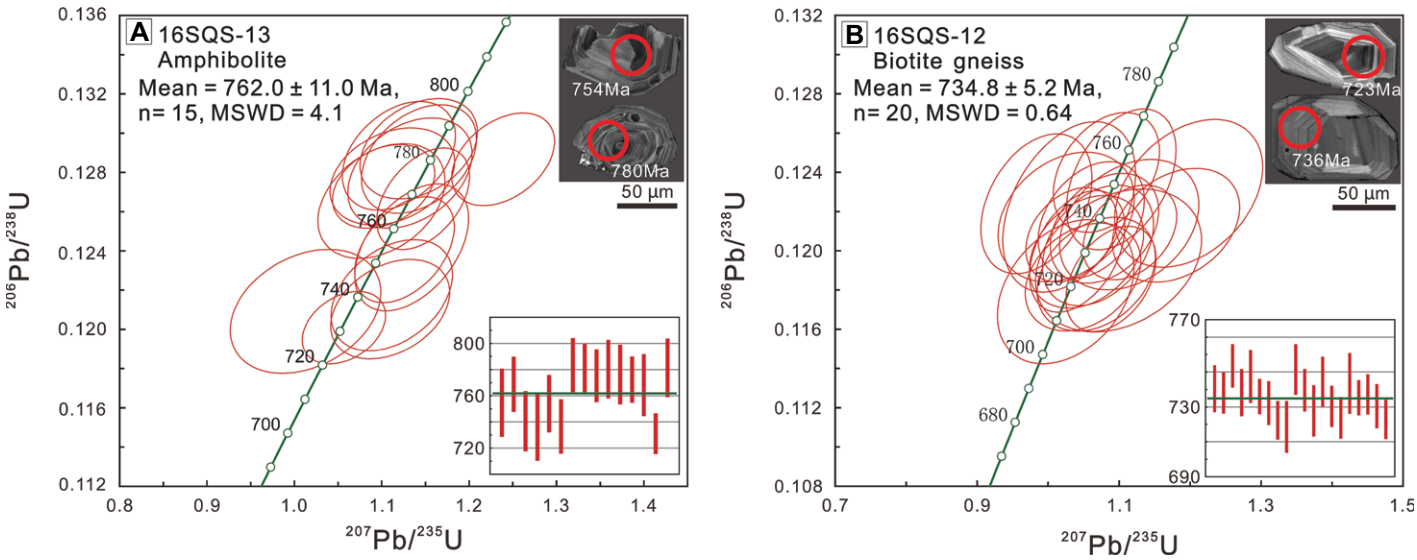

Figure 7. Laser ablation–inductively coupled plasma–mass spectrometry zircon U-Pb concordia diagrams and weighted mean plots for various host rocks in the Shuangqishan gold deposit of southeastern China. (A) Amphibolite (sample 16SQS-13); (B) biotite gneiss (sample 16SQS-12). MSWD—mean square weighted deviation; n—number of the spot analysis.

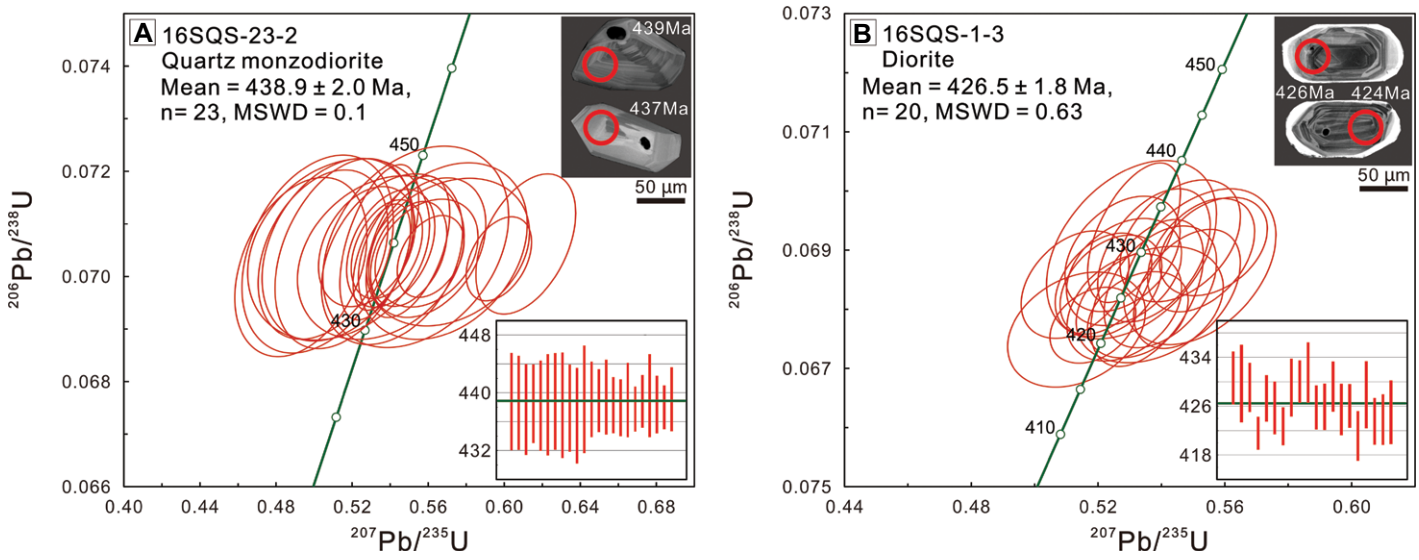

Figure 8. Zircon U-Pb concordia and weighted mean plots for magmatic rock samples from the Shuangqishan gold deposit of southeastern China. (A) Quartz monzodiorite (Sample 16SQS23-2); (B) diorite dike (Sample 16SQS1-3). MSWD—mean square weighted deviation; n—number of the spot analysis.

rather than metamorphic xenocrysts trapped in the gold lodes. In addition, the characteristic MREE-enriched patterns with apparent positive Eu anomalies recorded by Ap2 and Ap3 (Figs. 12C and 12D) are consistent with those in typical orogenic Au deposits (e.g., Brugger et al., 2000; Zheng et al., 2022), further supporting a hydrothermal origin of Ap2 and Ap3.

5.1.2. Trace Elements in Apatite and their Significance for Fluid Evolution

Apatite can effectively incorporate numerous trace elements in its structure (Pan and Fleet, 2002). Variations in trace element concentrations within apatite reflect changes in the fluid evolution (e.g., Andersson et al., 2019; Palma et al., 2019). These variations can be attributed to (1) changes in the composition of the hydrothermal fluid (Belousova et al., 2002); (2) changes in physicochemical conditions (e.g., pH, oxidation and sulfidation states, and temperature) of the hydrothermal system (Bath et al., 2013); (3) the partitioning of trace elements between various coevally crystallizing minerals (Andersson et al., 2019); and (4) compositional characteristics inherited from the country rocks (Ma et al., 2022a).

Significant variations in trace element abundances, especially the Mn, As, REE, Sr, and Y concentrations, were observed among different apatite generations (Figs. 11–13). Apatite from the quartz vein system of the Shuangqishan lode Au deposit shows middle REE (MREE)-enriched patterns with variable Eu anomalies (Fig. 12). The MREE-enriched patterns are consistent with the experimental study of Watson and Green (1981), which showed that the MREE is more compatible in apatite than the light and heavy REE.

Eu anomalies, either negative or positive, might be inherited from the hydrothermal fluids, or they can be derived from changes in the oxidation state (i.e., Eu^{2+} versus Eu^{3+}) of the dissolved Eu (Sverjensky, 1984). The distinct Eu anomalies exhibited by the metamorphic (Ap1) and hydrothermal (Ap2 and Ap3) apatite make it possible to discriminate between these two processes (Fig. 12). Previous thermodynamic modeling has indicated that over ~250 °C, under metamorphic or hydrothermal conditions, any Eu in an aqueous phase should be divalent (i.e., Eu^{2+}; Sverjensky, 1984). Ma et al. (2021) found that metamorphic and Au-mineralized hydrothermal quartz veins were formed at 320–340 °C and 250–310 °C, respectively. Consequently, all the Eu in the metamorphic fluids and ore-forming solutions should have been divalent. Apatite should favor trivalent europium relative to Eu^{2+} (Watson and Green, 1981). Furthermore, the ore-hosting metamorphic rocks show weak to prominent negative Eu anomalies (Zhang et al., 2005). Therefore, we propose that Ap1 was deposited from metamorphic fluids containing Eu^{2+} and that the negative Eu anomalies were inherited from the fluid. Trivalent cerium and Mn^{2+} are more easily incorporated into the structure of apatite than their quadrivalent forms (Belousova et al., 2002). Therefore, the relatively low manganese contents in the Ap2 and Ap3 compared to Ap1 (Fig. 10) suggest that they precipitated from fluids in which Mn was present in its oxidized state as Mn^{4+}. The apparent negative correlation between Eu/Eu* and Ce/Ce* displayed by different apatite generations also suggests that the auriferous fluids from which Ap2 and Ap3 crystallized were relatively oxidized compared to the pre-mineralization metamorphic fluid.

Another possible interpretation of the high Eu/Eu* values (>1) is that Ap2 and Ap3 inherited the positive Eu anomaly from plagioclase and/or sericitic alteration of the feldspars in the wall rocks (e.g., Ma et al., 2022a). As the REEs are highly incompatible with muscovite (Adam and Green, 2006), the contemporary apatite grains would readily accommodate any REE released through feldspar breakdown. Furthermore, the sericitization of feldspars and the chloritic alteration of amphibole could release significant amounts of Sr into the ore fluids (e.g., Xiao and Chen, 2020). Thus, a progressive reaction between the infiltrating ore-forming fluids and local host rocks and continuous breakdown of feldspars and amphibole likely resulted in the gradual accumulation of Sr in hydrothermal Ap2 and Ap3. As shown in Figure 13F, the variable $^{87}Sr/^{86}Sr$ ratios and Eu/Eu* values of the hydrothermal Ap2 and Ap3 define a binary mixing model probably involving ore-forming fluids and host rocks as two end-members (see below). As the change in oxygen fugacity could not affect the $^{87}Sr/^{86}Sr$ ratios recorded by apatite, we suggest that the decomposition of plagioclase in the surrounding wall rocks is the most critical mechanism that caused the apatite's Eu anomalies at Shuangqishan. Incorporation of As into apatite's texture is also redox-sensitive, and $(As^{5+}O_4)^{3-}$ prefers to substitute stoichiometrically for PO_4^{3-} in apatite compared to As^{3+}, which is accommodated

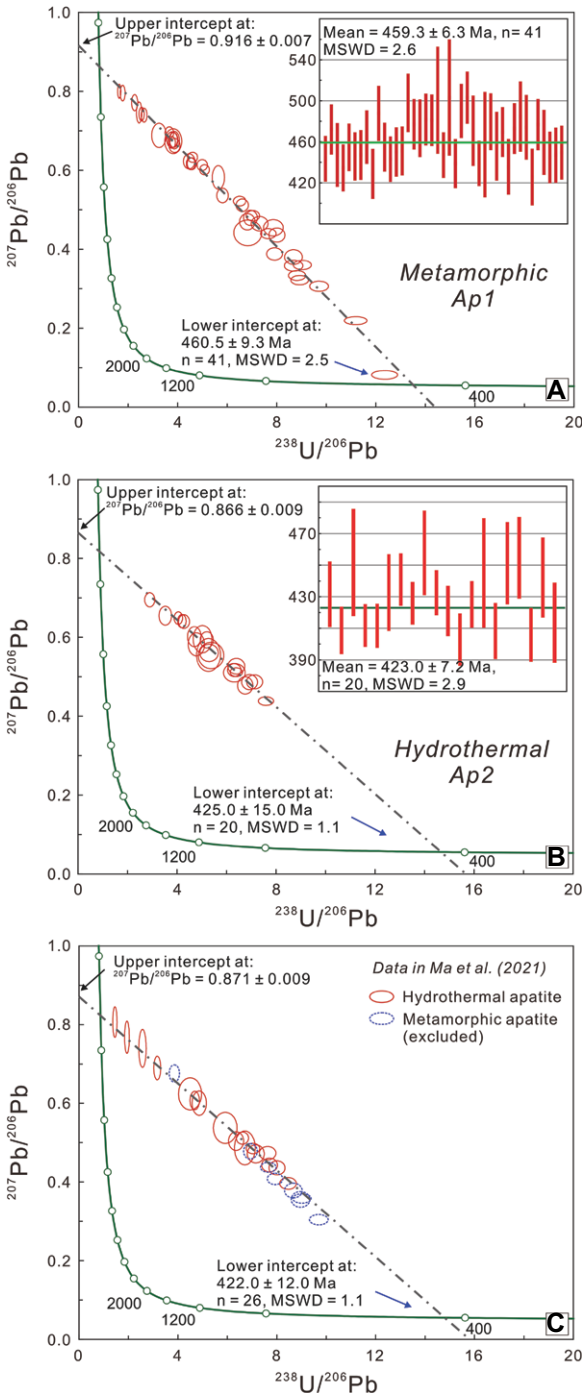

Figure 9. Tera-Wasserburg U-Pb plot for metamorphic apatite (Ap1) (A) and hydrothermal apatite (Ap2) (B and C) from the Shuangqishan deposit of southeastern China. The data for Figure 9C are from Ma et al. (2021). MSWD—mean square weighted deviation; n—number of the spot analysis.

in (arseno)sulfides (Liu et al., 2017). As such, low As contents recorded in apatite might reflect low As^{5+}/As^{3+} in a reducing circumstance or early precipitation of As-bearing sulfide minerals. As volcano-sedimentary rocks are generally enriched in As, which can then be released from the protoliths during regional metamorphism (e.g., Pitcairn et al., 2021), we propose that the elevated As concentrations in Ap1 are consistent with their metamorphic origin. The low As concentrations displayed by hydrothermal Ap2 and Ap3 coincide with their paragenetically simultaneous or late features compared to As-bearing pyrite (Figs. 5D and 5E; Ma et al., 2022c) rather than reflect the redox state of the ore fluids.

5.2. Timing of Metamorphism, Hydrothermal Activity, and Au Mineralization

A substantial effort has been made to constrain the timing of gold mineralization in the Shuangqishan deposit, mainly using Rb-Sr methods. Early studies employed Rb-Sr dating of fluid inclusions in quartz veins or chlorite in host rocks and yielded a broad range of early Paleozoic to Late Jurassic ages (e.g., Huang, 2001; Wu, 2002). The presence of multiple generations of fluid inclusions, including secondary ones in the quartz samples, may account for the large variations in their Rb-Sr ages (Ma et al., 2021). More recently, Bao et al. (2021) reported a Rb-Sr isochron age of 154 ± 2 Ma for pyrite from quartz veins at the Shuangqishan mine, and they interpreted it to reflect the age of the mineralization. However, neither Rb nor Sr are typically present in the pyrite structure but more likely reflect minute mineral inclusions within pyrite. Thus, the ages obtained on them do not necessarily date gold mineralization. Additionally, the complex textures exhibited by Shuangqishan's auriferous pyrite indicate that it experienced a complicated formation and deformation history (Ma et al., 2022c). Consequently, Rb-Sr age data derived using bulk analysis probably represent a mixed-signal, from which no geologically meaningful age can be obtained. In the light of the implicit limitation of Rb-Sr dating and the obvious age differences among samples from one single mine, the geological meaning of these Rb-Sr data are very unconvincing.

LA-ICP-MS U-Th-Pb geochronology has been utilized to constrain the age of the host rocks, mafic and granitic rocks, and of the Au mineralization in the Shuangqishan deposit, as well as the timing of regional-scale metamorphic, magmatic, and hydrothermal activities associated with the emplacement of the barren and auriferous quartz veins (Fig. 14).

(Meta)volcanic rocks of the Daling Formation were formed between ca. 758 and 721 Ma (Wan et al., 2007). The U-Pb dates of 762.0 ± 11.0 Ma and 734.8 ± 5.2 Ma (Fig. 7) determined on zircon grains from the amphibolite and biotite gneiss in this study are construed as igneous crystallization ages, which are apparent igneous and lack evidence of significant dissolution or other post-precipitation alteration (Fig. 7). These ages are consistent with previous geochronological data (Wan et al., 2007) and confirm a late Neoproterozoic (Tonian) age for the Daling Formation, which hosts the Shuangqishan Au deposit. Previous geochronological studies for the Caledonian Orogen in the eastern Cathaysia Block indicate that the peak metamorphism and the principal deformation episodes took place during ca. 460–440 Ma (Li et al., 2010). The age of 460.5 ± 9.3 Ma obtained in this study for euhedral Ap1 of Stage I (Fig. 9A) now provides a direct age of the metamorphism in the Shuangqishan area.

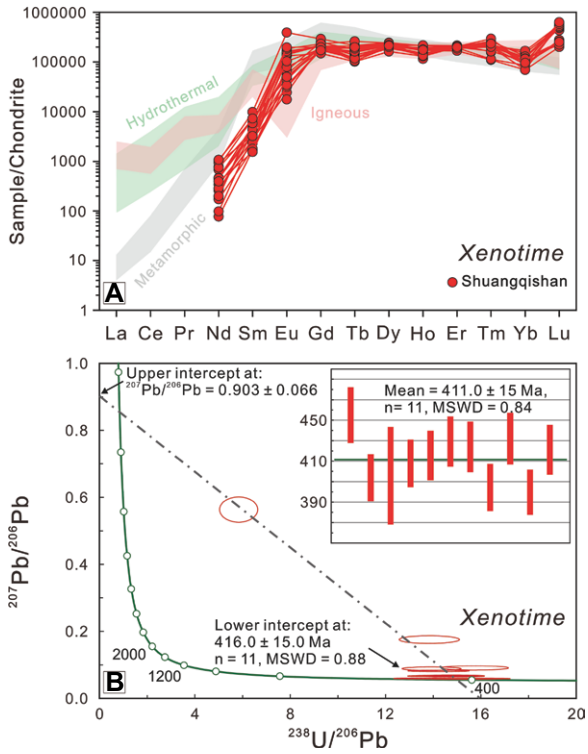

Figure 10. (A) Chondrite-normalized rare earth element distribution in hydrothermal xenotime from the Shuangqishan gold deposit of southeastern China with compositions from hydrothermal (Kositcin et al., 2003; Taylor et al., 2015), igneous (Kositcin et al., 2003), and metamorphic (Aleinikoff et al., 2012, 2015) environments. (B) Tera-Wasserburg plot of gold-related hydrothermal xenotime from the Shuangqishan gold deposit. MSWD—mean square weighted deviation; n—number of the spot analysis.

Microthermometric data indicate that the temperature of hydrothermal fluids that form the auriferous quartz veins (~250–340 °C; Ma et al., 2021) in the Shuangqishan deposit are significantly lower than the closure temperatures of the U-Th-Pb systems in apatite (~550 °C; Kirkland et al., 2018) and xenotime (~900 °C; Cherniak, 2006). Resetting of the isotope clocks can thus be excluded and, consequently, our new age data should provide direct evidence of the age of gold mineralization, that is, 425.0 ± 6.3 Ma and 422.0 ± 12.0 Ma (Figs. 9B and 9C).

Characterization based on textures and SEM images indicates that the vein-hosted xenotime analyzed in this study is hydrothermal in origin. All xenotime crystals analyzed exhibit hypidiomorphic to xenomorphic morphology and filled the micro-fractures or occurred as inclusions in brecciated or fractured pyrite and chalcopyrite, indicating that this xenotime was precipitated simultaneously or shortly after pyrite and chalcopyrite (Fig. 6). REE abundances in these xenotime grains are distinct from those typical of metamorphic and igneous xenotime (Fig. 10A). Hydrothermal xenotime has notably lower U and Th concentrations than published results for metamorphic and igneous xenotime (Table S6; Kositcin et al., 2003; Taylor et al., 2015). The REE distribution patterns of the xenotime reported here show no or slightly positive Eu anomalies, which are distinct from the igneous xenotime and exhibit remarkable negative Eu anomalies (Fig. 10A). Moreover, the REE patterns for Shuangqishan xenotime are different from those typical of metamorphic xenotime that shows enrichment in MREE (Fig. 10A). These petrologic and chemical traits illustrate that the xenotime analyzed in our study from Stage II auriferous quartz veins are hydrothermal in origin.

Gold mineralization in the Shuangqishan deposit mainly occurs as two distinct forms: Type I as visible rounded inclusions or invisible micro-inclusions within euhedral to subhedral pyrite crystals in sub-stage IIa quartz-pyrite veins (Fig. 4E); and type II as free gold ± Bi-Te phases ± chalcopyrite assemblages situated along microfractures of brecciated pyrite grains within sub-stage IIb quartz-chalcopyrite-pyrite veins (Fig. 4F; Ma et al., 2022c). As the euhedral to subhedral pyrite grains coexist with and contain, Ap2 grains dated at ca. 425 Ma, the sub-stage IIa gold (micro)inclusions in this pyrite are also suggested to have precipitated at this time. Sub-stage IIb pyrite grains containing veinlets of free gold (Fig. 4F), chalcopyrite, and Bi-Te phases, hydrothermal xenotime grains along pyrite grain boundaries or intergrown with chalcopyrite yielded an age of 416.0 ± 15.0 Ma (Fig. 10B). The in situ U-Pb isotope ages of sub-stage IIa hydrothermal Ap2 and sub-stage IIb hydrothermal xenotime obtained in this study are mutually consistent and within the error range. Thus, the present apatite and xenotime U-Pb ages indicate that both the refractory- (sub-stage IIa) and free-gold (sub-stage IIb) mineralization are the product of one and the same mineralizing event (Fig. 14).

5.3. Constraints on Fluid Evolution by Apatite Sr Isotopes

A detailed investigation of the paragenetic sequence and isotope signatures of apatite unravels an evolutional history of the Sr isotopic compositions of the fluids. Unaltered metasedimentary (quartz-mica schist and biotite gneiss) and metaigneous (amphibolite) rocks of the Neoproterozoic basements in Fujian have age-corrected $^{87}Sr/^{86}Sr$ ratios of 0.7326–0.7634 and 0.7075–0.7130, respectively (Fig. 15; Yuan et al., 1991). On the other hand, the metamorphic Ap1 shows the most radiogenic Sr isotopic ratios from 0.7178 to 0.7302 among all apatite generations. These ratios lie between those of regional Neoproterozoic metasedimentary and metaigneous rocks (Fig. 15). Taking into account the syn-metamorphic age of Ap1, we suggest that the variable and highly radiogenic $^{87}Sr/^{86}Sr$ ratios of Ap1 may reflect an uneven mixing of metasedimentary- and metaigneous-derived metamorphic fluids.

Hydrothermal Ap2 and Ap3 have $^{87}Sr/^{86}Sr$ ratios of 0.7100–0.1765 and 0.7086–0.7116, respectively, significantly lower than those in metamorphic Ap1 (Fig. 15). The significant time gap of ~35 ± 24 m.y. between the crystallization of Ap2 and Ap1, together with the distinct $^{87}Sr/^{86}Sr$ values of these two generations of apatite, negate the hypothesis that the ore-forming fluids were derived from the metamorphism of supracrustal rocks. Additionally, Ap3 generally has higher Sr concentrations but less radiogenic Sr isotopic ratios than Ap2. The Sr isotopic compositions of Ap2 and Ap3 are different from those in the ca. 438 Ma quartz monzodiorite in the mine area (~0.7240; unpublished data), the ca. 441–427 Ma gabbro and diorite in the surrounding regions (0.7066–0.7104; Zhang et al., 2015), and other known Sr reservoirs (Fig. 15).

Fluid-wall rock interaction represents a common process in orogenic gold deposits and has the potential to affect fluid Sr isotope compositions (Glodny and Grauert, 2009; Scanlan et al., 2018). Given the widespread sericitization and chloritization around the auriferous quartz veins (Ma et al., 2021), the Sr isotopic ratios of Ap2 and Ap3 most likely reflect a mixing of hydrothermal fluid- and wall-rock-derived Sr. This interpretation is also supported by the apparent mixing trend displayed in the Eu/Eu* versus $^{87}Sr/^{86}Sr$ diagram (Fig. 13F). The host rocks of the Shuangqishan deposit are quartz-mica schist with interlayered mafic to felsic metavolcanic rocks of the Daling Formation. At the time of gold mineralization, the quartz-mica schist and

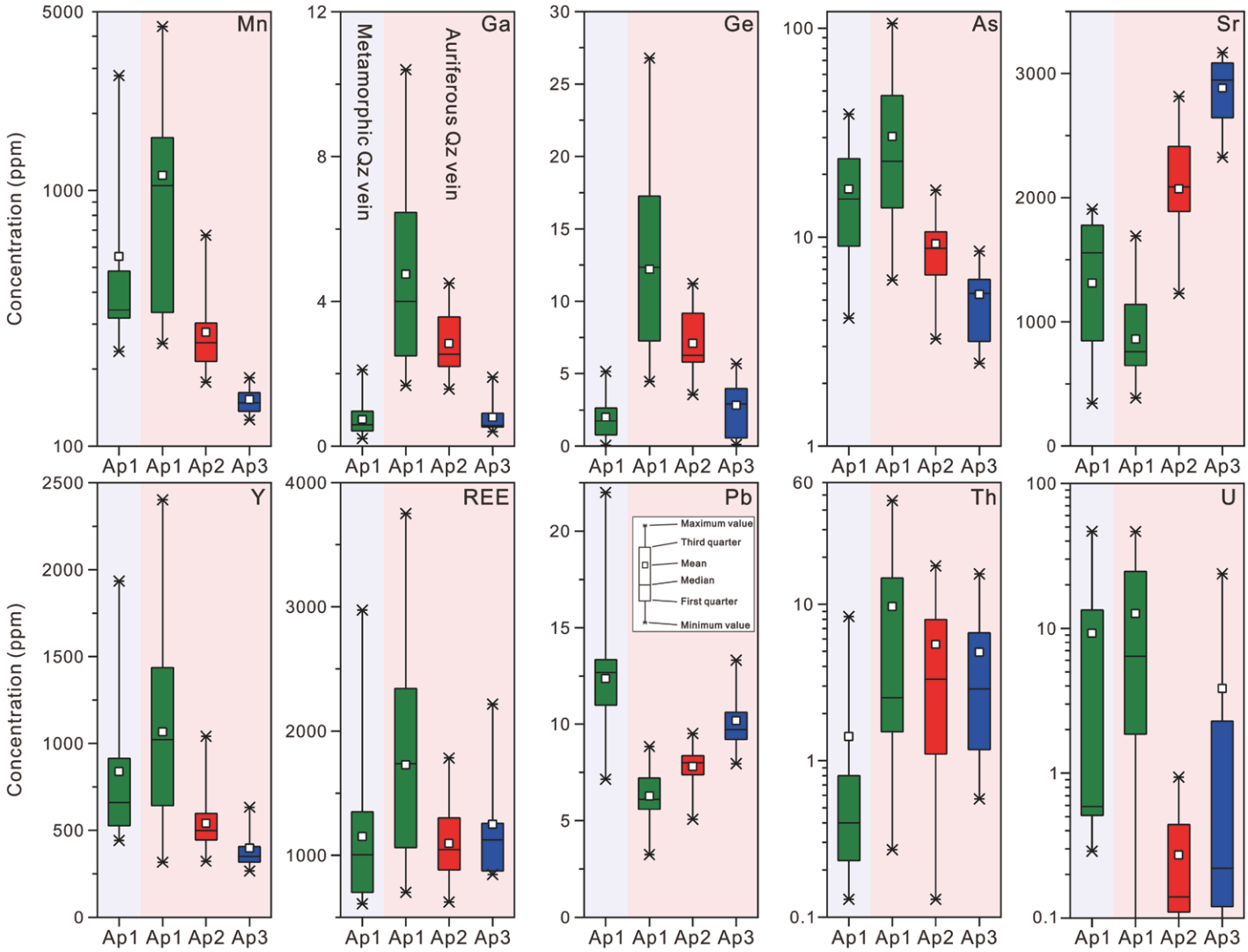

Figure 11. Diagrams showing the contents of selected trace elements in different types of apatite in the Shuangqishan gold deposit of southeastern Chin. Qz—quartz; REE—rare earth element.

metavolcanic rocks have Sr isotope compositions of 0.7326–0.7634 and 0.7075–0.7130, respectively (Yuan et al., 1991). The $^{87}Sr/^{86}Sr$ ratios of Ap2 and Ap3 lie between those in metasedimentary and metavolcanic members of the host rocks but much closer to the metavolcanic wall rocks. The quartz-mica schist mainly consists of quartz and muscovite that are free of Sr, and it could not provide much Sr during fluid-rock interaction. Thus, the plagioclase and amphibole of the amphibolite, as well as the plagioclase of the biotite gneiss, are likely sources of Sr through fluid-wall rock reaction. The Ap2 grain with the lowest Sr content but highest $^{87}Sr/^{86}Sr$ ratio (0.7156) should undergo the fluid-wall rock exchange at the lowest degree (Fig. 13F) and has the Sr isotope ratio that is most close to the ore-forming fluids. However, this value is distinct from all the known Sr reservoirs in the Shuangqishan area (Fig. 15). Previous study suggested that the ore-forming fluids of the Shuangqishan deposit are deep-seated either magmatic- or mantle-derived fluids (Bao et al., 2021; Ma et al., 2021). This means the Au-bearing fluids must experience a long-distance ascent until precipitated in the Shuangqishan shear zone. In addition, pervasive fluid-rock interaction during the transportation of auriferous fluids through various lithologies in the pathways may modify the Sr isotope compositions of the fluids. As such, the fluids that precipitated the gold ores could have different $^{87}Sr/^{86}Sr$ ratios to their source regions. In summary, apatite $^{87}Sr/^{86}Sr$ ratios do not pinpoint a precise origin to the ore-forming fluids, and the distinct $^{87}Sr/^{86}Sr$ values recorded by Ap2 and Ap3 may reflect the different degrees of isotopic equilibration between country rocks and ore-forming fluids through hydrothermal evolution.

5.4. Genetic Model for the Shuangqishan Orogenic Gold Deposit

The origin of the Shuangqishan gold deposit has been debated, with sub-crustal to supracrustal metamorphic or magmatogenic processes suggested (e.g., Li, 2010; Ma et al., 2021). Armed with new geochronological results and observations presented here and data from previous research, we now carefully reexamine the existing genetic models of the Shuangqishan deposit. The apparent difference between our new hydrothermal apatite and xenotime U-Pb dates and previous radiometric ages for the gold lodes illustrates that the Yanshanian intrusion-related model (Li, 2010; Bao et al., 2021) can be precluded. Much evidence suggests an amphibolite-facies crustal metamorphic fluid source with metals from Neoproterozoic basement rocks during

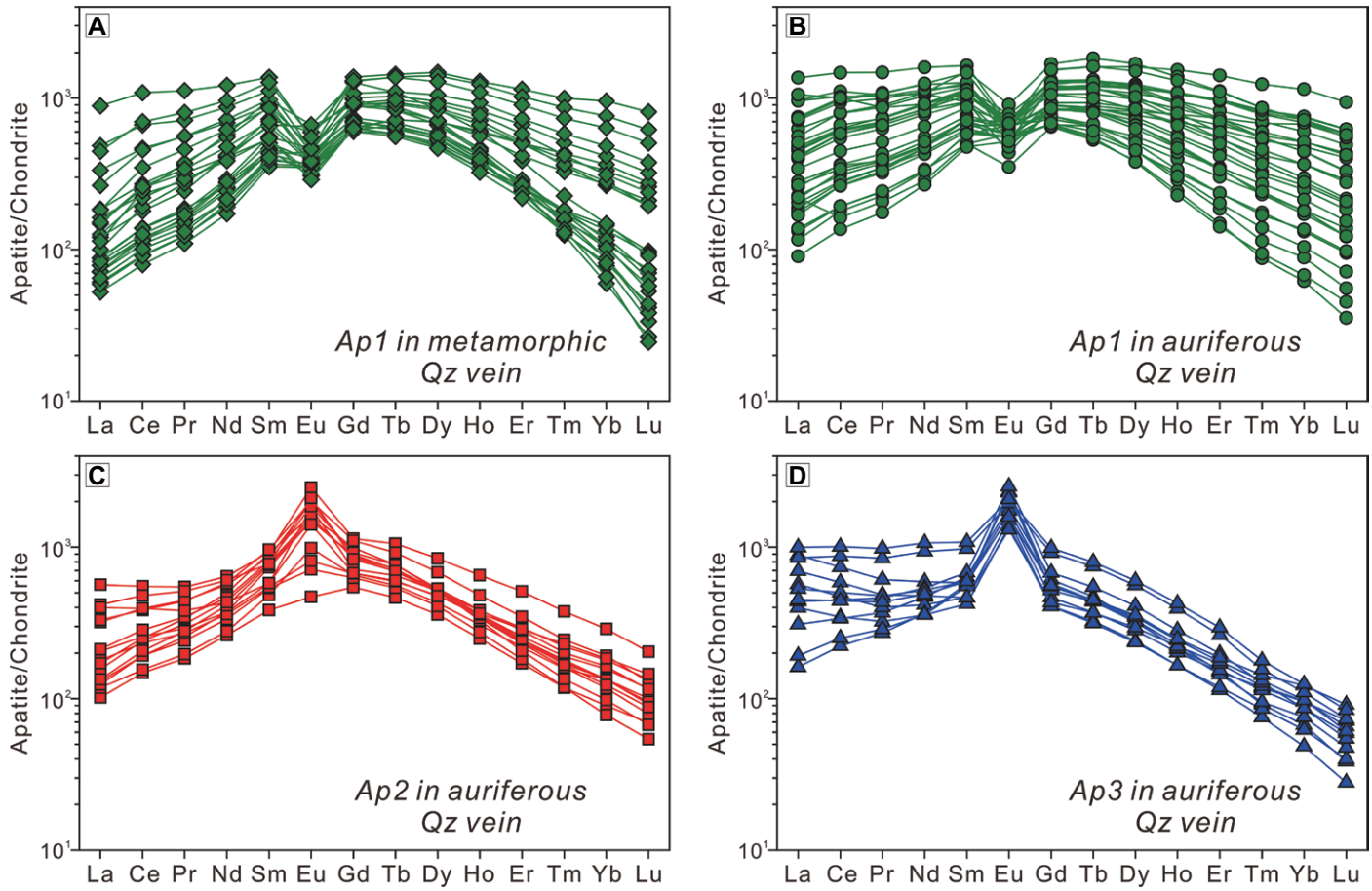

Figure 12. Chondrite-normalized rare earth element patterns (normalization values are from McDonough and Sun, 1995) of apatite grains from the Shuangqishan gold deposit of southeastern China. Qz—quartz.

the Caledonian Orogeny (Kou et al., 2016; Yuan and Chen, 2015). Our new apatite U-Pb age data reveal that the amphibolite-facies metamorphism in Shuangqishan and surrounding areas occurred in the Middle Ordovician (ca. 461 Ma), approximately 35 ± 24 m.y. prior to the Late Silurian (ca. 425 Ma) gold mineralization. Thus, a crustal metamorphic model from local host rocks can be ruled out, and the formation of Shuangqishan requires external sources of fluids and sulfur.

Our new LA-ICP-MS zircon U-Pb data indicate that the quartz monzodiorite in the mining district was emplaced at 439 ± 2 Ma and predates mineralization of the Shuangqishan deposit by 14 ± 17 m.y. The large age gap between the formation of the hydrothermal proto-ores in the Shuangqishan deposit and emplacement of spatially related granite weakens the possibility that the ore-forming fluids were derived from igneous degassing. There is also a lack of fluid inclusion microthermometric data to illustrate magmatic-hydrothermal temperatures (over 500 °C) and salinities, and no indication of alteration or metal zonation, typical of granitic intrusion-related gold deposits. As Ma et al. (2021, 2022c) demonstrated, the potassic-dominated country-rock alteration, strong structural control on gold veins, CO_2-rich, mediate temperature and low- to mediate-salinity ore fluids, trace element contents of auriferous pyrite, and stable and radiogenic isotope compositions all resemble those of typical orogenic gold deposits (Groves, 1993; Goldfarb et al., 2005).

As the crustal metamorphic devolatilization from local host rocks and granite-related hydrothermal models have been discounted, we suggest that devolatilization during metamorphism of the deeper-seated basement rocks that previously metamorphosed at sub-greenschist to greenschist phase or a sub-crustal source generated from a fertilized mantle lithosphere are the possible sources of the auriferous fluids in the Shuangqishan orogenic gold deposit (Ma et al., 2021). A diorite dike in the mine area was emplaced at ca. 427 ± 2 Ma, and a gabbro intrusion in the broader region was dated at 441–431 Ma (Zhang et al., 2015). These ages are broadly consistent with the timing of gold mineralization in the Shuangqishan gold deposit (ca. 425 Ma), suggesting that the devolatilization of mafic magmas or mantle-derived volatiles may have contributed to the ore-forming fluids. A mantle origin of the Shuangqishan gold deposit is supported by the magmatic-like H-O isotope compositions of ore-forming fluids ($\delta^{18}O_{fluid} = 4.8‰–8.0‰$, $\delta D = -84‰$ to $-51‰$; Ma et al., 2021). The elevated $^3He/^4He$ ratios (0.06–0.23 Ra; Ma et al., 2021) relative to purely crustal He reservoirs ($^3He/^4He < 0.01$ Ra) further reveal the presence of a mantle-derived component in the hydrothermal system. Sulfur isotope data ($\delta^{34}S_{V\text{-}CDT}$ (Vienna-Canyon Diablo Troilite) $= -7.9‰$ to $-0.1‰$; Ma et al., 2022c) provide additional evidence for a mantle source of sulfur. Negative $\delta^{34}S_{V\text{-}CDT}$ ratios likely reflect isotopic fractionation caused by the oxidation of mantle-derived fluids (Ohmoto, 1972; Ma et al., 2022c). The occurrence of Au-associated Bi-Te minerals in the quartz-sulfide veins also points to a mantle origin of at least some metals (Bi et al., 2011; Ma et al., 2022c). Apatite $^{87}Sr/^{86}Sr$ ratios do not point to a precise source of the ore-forming fluids as it is probable that the Sr isotope signature of the fluid was partly or totally overprinted by fluid-rock interaction during fluid

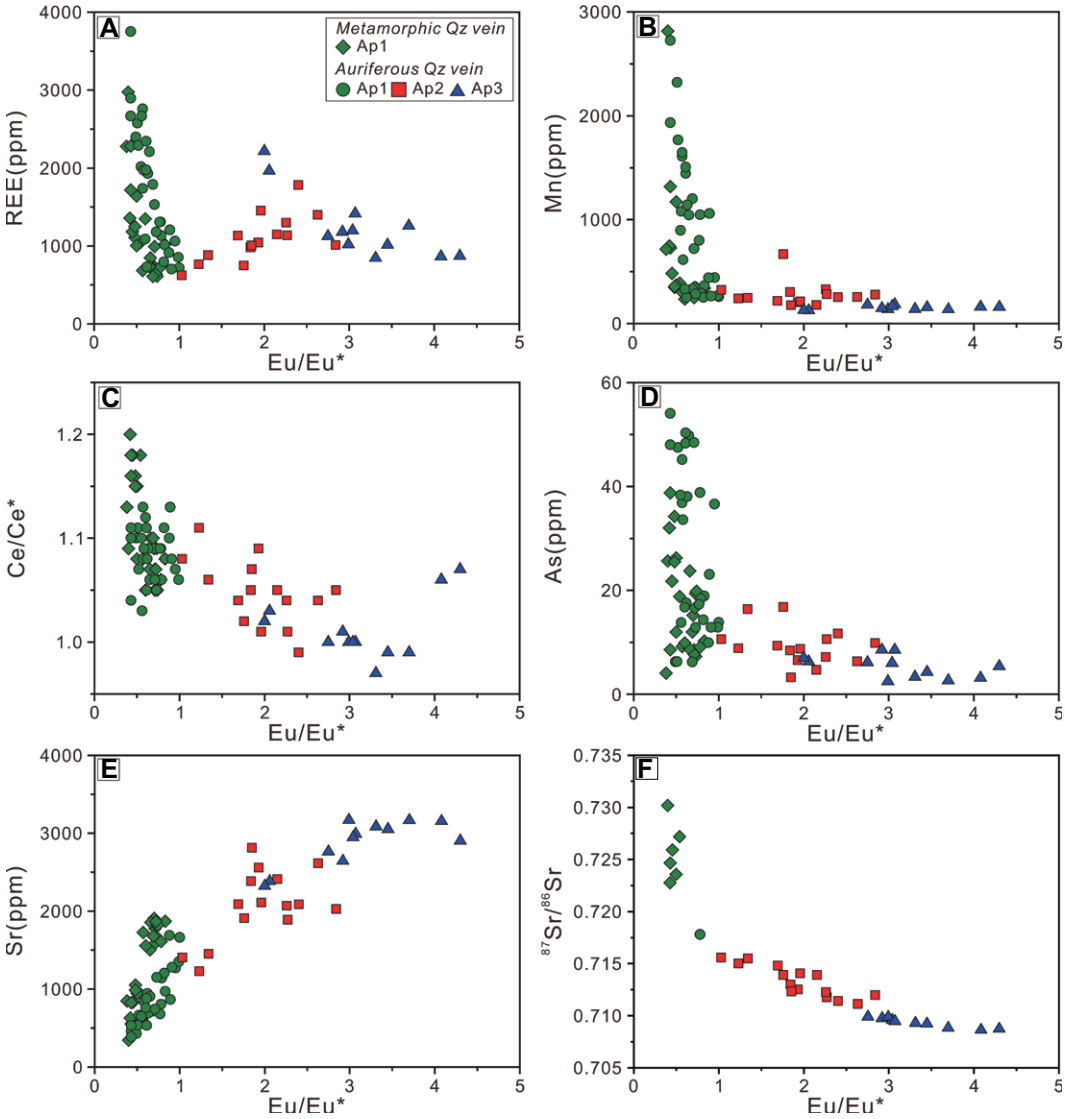

Figure 13. Scatter diagrams of trace elements and $^{87}Sr/^{86}Sr$ ratios for different apatite generations in the Shuangqishan gold deposit of southeastern China. (A) Rare earth element (REE) versus Eu/Eu*; (B) Mn versus Eu/Eu*; (C) Ce/Ce* versus Eu/Eu*; (D) As versus Eu/Eu*; (E) Sr versus Eu/Eu*; and (F) $^{87}Sr/^{86}Sr$ versus Mn. Qz—quartz.

ascent. Nevertheless, the Shuangqishan's hydrothermal apatite Sr isotope data set suggests that Sr and, by inference, the fluids that carried gold were derived from an external, deeply sourced reservoir rather than locally sourced from metamorphic dewatering of the ore-hosting volcanosedimentary sequence.

The evolution of metamorphic and ore-forming fluids in the Shuangqishan deposit is shown in Figure 16. The barren and auriferous quartz veins and the apatite within them were precipitated from fluids with distinct sources. Temporal variations of Sr isotope ratios in these fluids are not only controlled by their fluid sources but also by the influence of wall rock components.

5.5. Global Implications

The age of lode gold deposits, as best exemplified by orogenic and intrusion-related Au deposits, should be concisely constrained to decipher the relationship of gold mineralization to a tectonic framework (Groves, 1993; Goldfarb et al., 2005). Apatite has been reported as a minor hydrothermal phase in many orogenic gold deposits formed in a wide range of temperatures, from as low as 300 °C (e.g., Sigma and Sicore deposits in the Val d'Or Au district of Canada, Robert and Brown, 1986; Loulo mining district in Mali of West Africa, Lawrence et al., 2013; Pau-a-Pique and Ernesto deposits in the Alto Guaporé Au province of Brazil, de Melo, 2022), through to moderate temperatures at upper greenschist- and lower amphibolite-facies conditions (e.g., Giant mine in the Canadian shield, Tindals mine in Yilgarn Craton of Australia, Sciuba and Beaudoin, 2021; Hutti mine in Dharwar Craton of India, Hazarika et al., 2016), and high temperatures (>600 °C; e.g., Tropicana deposit in Yilgarn Craton of Australia, Crawford and Doyle, 2016). Apatite has also been recognized in many intrusion-related gold deposits, such as the Björkdal deposit in Sweden (Roberts et al., 2006), Myrtle Creek deposit in the Stawell goldfields of Australia (Bierlein and McKnight, 2005), and Morila deposit in Mali (McFarlane et al., 2011), in which it exhibits close association with ore and gangue minerals. Our work illustrates that apatite in orogenic gold systems can hold parts-per-million-level, lattice-bound U, which is sufficient to generate precise U-Pb ages. Consequently, the common presence of apatite closely associated with gold and gold-related phases in many orogenic and intrusion-related gold systems makes it a possible U-Pb geochronometer for lode gold deposits. However, based on our observations, in the case of Shuangqishan, up to three generations of apatite could be identified even within a single grain in the auriferous quartz veins, and their genesis could be linked

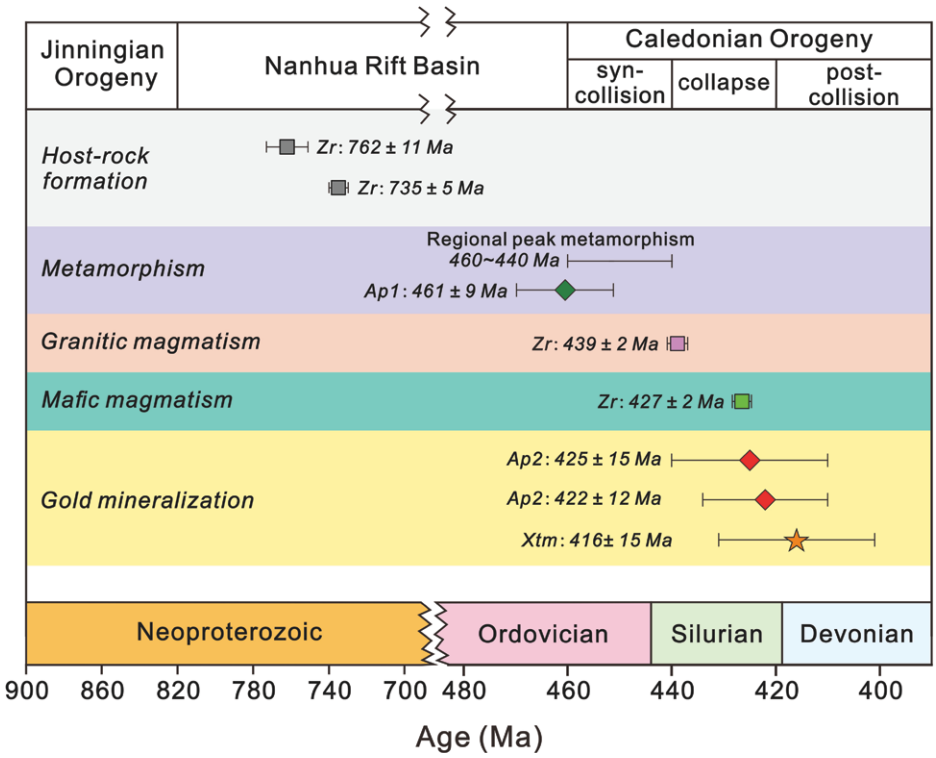

Figure 14. Timelines showing the age of gold mineralization at Shuangqishan in southeastern China in relation to some major tectonic, metamorphic, and magmatic events in the Caledonian Orogen of southeastern China. Xtm—xenotime.

to different geological events. As such, careful textural examination plus in situ trace element analysis based on robust geological evidence are indeed necessary and are highly recommended to ascertain the proper origin of the apatite before geochronological investigations.

The utilization of apatite Sr isotope compositions is becoming more and more popular globally due to the presence of apatite in diverse mineral deposit types (e.g., Mao et al., 2016). Studies on magmatic-hydrothermal apatite from Austria and China has identified a wide range of $^{87}Sr/^{86}Sr$ ratios within a single deposit (e.g., Zhao et al., 2015; Kozlik et al., 2016). However, information on the $^{87}Sr/^{86}Sr$ ratios of apatite in orogenic gold deposits remains scarce; only one recent study on metasomatic apatite in the Xindigou orogenic Au deposit in China reveals a complex Sr source for its formation (Zhang et al., 2020). Similar to these deposits, the Shuangqishan $^{87}Sr/^{86}Sr$ data show the apatite to mostly be heterogeneous, varied on a sample (thin section) to deposit scale. Deposits with such $^{87}Sr/^{86}Sr$ characteristics can be attributed to (1) polystage formation history of the deposit by hydrothermal fluids with isotopically different sources (Kozlik et al., 2016); (2) mixing of multiple fluids with different Sr isotope signatures (Lüders et al., 2009); or (3) modification of the $^{87}Sr/^{86}Sr$ ratios in ore fluids during infiltration of chemical inhomogeneous lithologies-derived Sr (Glodny and Grauert, 2009). In the Shuangqishan system, the wall rocks contain metavolcanic and metasedimentary components with distinct $^{87}Sr/^{86}Sr$ ratios, and various degrees of isotopic equilibration between country rock and sub-crustal-derived ore-forming fluids led to the heterogeneous Sr isotope compositions preserved in apatite.

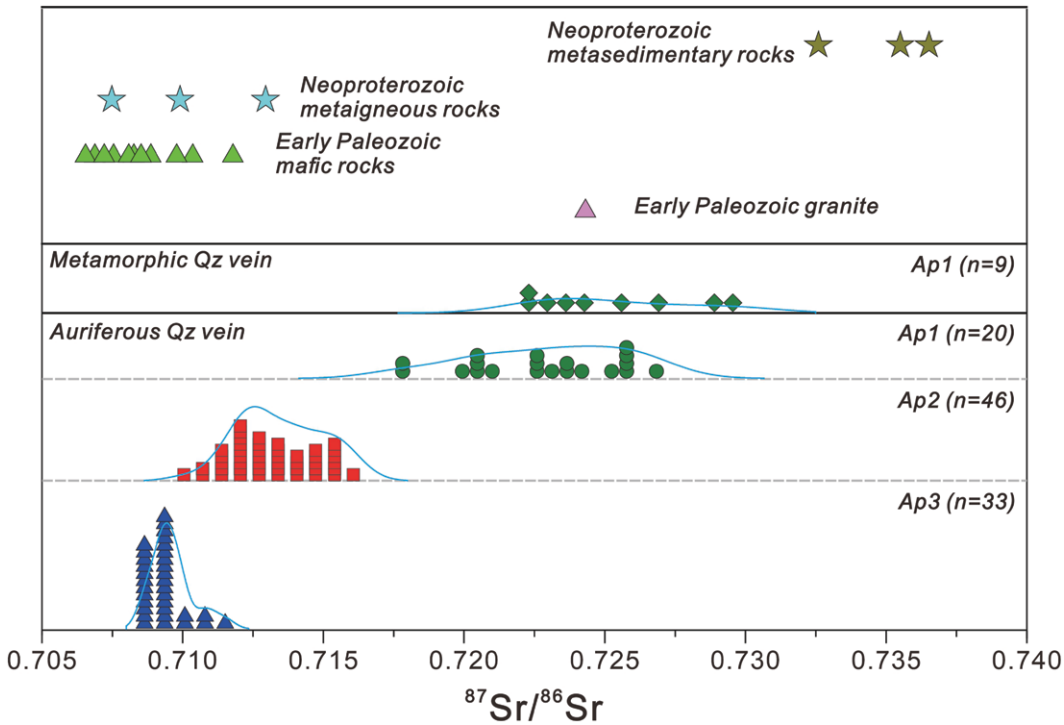

Figure 15. $^{87}Sr/^{86}Sr$ ratios of apatite and calcite from different paragenetic stages in the Shuangqishan gold deposit of southeastern China. Probability density plots are shown above the data points. Qz—quartz.

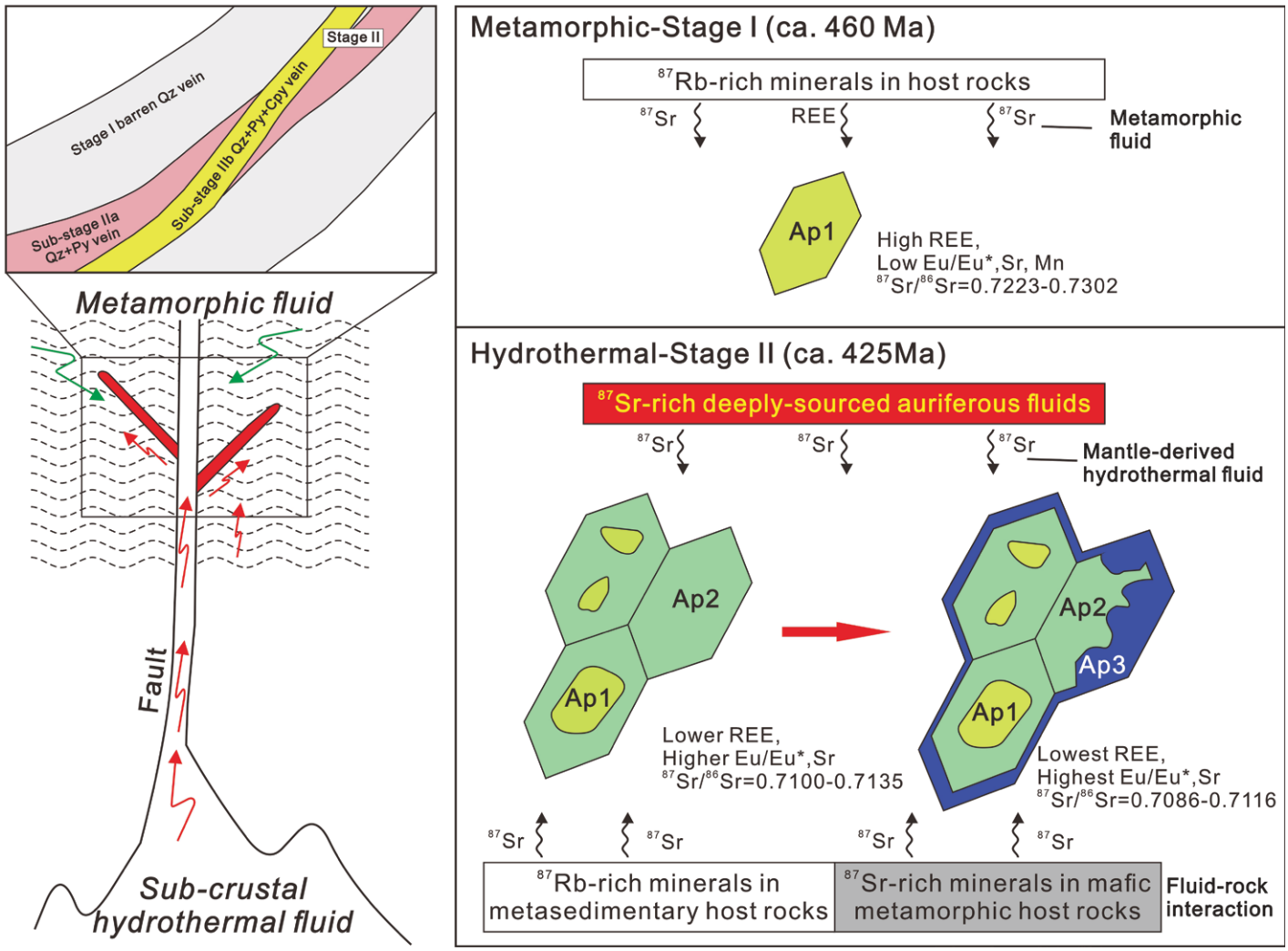

Figure 16. Schematic cartoon showing the metamorphic and hydrothermal stages of apatite formation in the Shuangqishan gold deposit of southeastern China. See text for exploration. Qz—quartz; Py—pyrite; Cpy—chalcopyrite; REE—rare earth element.

6. CONCLUSIONS

In this study, we utilized detailed petrographic examination and in situ analyses of apatite along with evidence from zircon and xenotime geochronological data to better understand the age and complex mineralization history of an orogenic gold deposit. Our work demonstrates that apatite is a potential geochronometer for lode gold deposits and apatite chemistry might serve as a reliable proxy for elucidating the complicated ore-forming processes and evaluating the influence of fluid-rock interaction within mineral deposits.

The OP-CL imaging revealed three generations of apatite (Ap1 to Ap3) within metamorphic and gold-mineralized quartz veins. These apatite generations have different trace element characteristics that reflect a change in fluid compositions and an increase in oxidation state from metamorphic to gold-forming hydrothermal stages. The high Sr content of hydrothermal apatite was most likely derived from the breakdown of plagioclase and amphibole during the hydrothermal evolution. The Sr isotope composition in apatite reflects the mixing of fluid-derived and host rock-derived Sr. Consequently, different degrees of isotopic equilibration between wall rock and hydrothermal fluids could be responsible for the various $^{87}Sr/^{86}Sr$ values in hydrothermal apatite.

Hydrothermal Ap2 and xenotime within the auriferous quartz-sulfide veins yielded identical U-Pb ages of 425 ± 15–416 ± 15 Ma, which constrain the gold mineralizing to the Late Silurian rather than to the Neoproterozoic or Late Jurassic–Early Cretaceous as previously suggested. It is at least 35 ± 24 m.y. younger than the regional metamorphism in the Middle Ordovician as indicated by the U-Pb age of Ap1 within pre-ore metamorphic quartz veins. In combination with independent geological and geochemical investigations, the results presented herein favor an orogenic genetic model linking to deeper-crustal or sub-crustal ore-forming fluids for the Shuangqishan gold deposit.

ACKNOWLEDGMENTS

This study was funded by the National Natural Science Foundation of China (41973044) and the MOST Special Fund from the State Key Laboratory of Geological Processes and Mineral Resources, China University of Geosciences (MSFGPMR03-2). We also appreciate the kind help of Dr. Bin Fu from the Australian National University (Canberra, Australia) on the sensitive high-resolution ion microprobe xenotime U-Pb isotope dating. This paper has been greatly improved by a thorough review from two anonymous reviewers, Associate Editor Haibo Zou, and Chief Editor Wenjiao Xiao.

REFERENCES CITED

Adam, J., and Green, T., 2006, Trace element partitioning between mica- and amphibole-bearing garnet lherzolite and hydrous basanitic melt: 1. Experimental results and the investigation of controls on partitioning behavior: Contributions to Mineralogy and Petrology, v. 152, p. 1–17, https://doi.org/10.1007/s00410-006-0085-4.

Aleinikoff, J.N., Hayes, T.S., Evans, K.V., Mazdab, F.K., Pillers, R.M., and Fanning, C.M., 2012, SHRIMP U-Pb ages of xenotime and monazite from the Spar Lake Red Bed-associated Cu-Ag deposit, Western Montana: Implications for ore genesis: Economic Geology, v. 107, p. 1251–1274, https://doi.org/10.2113/econgeo.107.6.1251.

Aleinikoff, J.N., Lund, K., and Fanning, C.M., 2015, SHRIMP U-Pb and REE data pertaining to the origins of xenotime in Belt Supergroup rocks: Evidence for ages of deposition, hydrothermal alteration, and metamorphism: Canadian Journal of Earth Sciences, v. 52, p. 722–745, https://doi.org/10.1139/cjes-2014-0239.

Andersson, S.S., Wagner, T., Jonsson, E., Fusswinkel, T., and Whitehouse, M.J., 2019, Apatite as a tracer of the source, chemistry and evolution of ore-forming fluids: The case of the Olserum-Djupedal REE-phosphate mineralisation, SE Sweden: Geochimica et Cosmochimica Acta, v. 255, p. 163–187, https://doi.org/10.1016/j.gca.2019.04.014.

Barker, S.L., Hickey, K.A., Dipple, G.M., and Layne, G., 2009, Apatite as a paleohydrothermal fluid recorder in Carlin-type gold deposits: American Geophysical Union Joint Assembly 2009, Toronto, Canada.

Bao, T., Ni, P., Li, S.N., Xiang, H.L., Wang, G.G., Chi, Z., Li, W.S., Ding, J.Y., and Dai, B.Z., 2020, Geological, fluid inclusion, and H-O-C-S-Pb isotopic constraints on the genesis of the Shuangqishan gold deposit, Fujian, China: Journal of Geochemical Exploration, v. 214, https://doi.org/10.1016/j.gexplo.2020.106544.

Bao, T., Ni, P., Dai, B.Z., Wang, G.G., Chen, H., Li, S.N., Chi, Z., Li, W.S., Ding, Y.J., and Chen, L.L., 2021, Pyrite Rb-Sr geochronology, LA-ICP-MS trace element and telluride mineralogy constraints on the genesis of the Shuangqishan gold deposit, Fujian, China: Ore Geology Reviews, v. 138, https://doi.org/10.1016/j.oregeorev.2021.104158.

Bath, B.A., Walshe, J.L., Cloutier, J., Verrall, M., Cleverley, J.S., Pownceby, M.I., Macraw, C.M., Wilson, N.C., Tunjic, J., Nortje, G.S., and Nortje, G.S., 2013, Biotite and apatite as tools for tracking pathways of oxidized fluids in the Archean East Repulse gold deposit, Australia: Economic Geology, v. 108, p. 667–690, https://doi.org/10.2113/econgeo.108.4.667.

Belousova E. A., Griffin W. L., O'Reilly S. Y. and Fisher N. I., 2002, Apatite as an indicator mineral for mineral exploration: trace-element compositions and their relationship to host rock type: Journal of Geochemical Exploration, v. 76, p. 45–69, https://doi.org/10.1016/S0375-6742(02)00204-2.

Bi, S.J., Li, J.W., Zhou, M.F., and Li, Z.K., 2011, Gold distribution in As-deficient pyrite and telluride mineralogy of the Yangzhaiyu gold deposit, Xiaoqinling district, southern North China craton: Mineralium Deposita, v. 46, p. 925–941, https://doi.org/10.1007/s00126-011-0359-2.

Bierlein, F.P., and McKnight, S., 2005, Possible intrusion-related gold systems in the western Lachlan Orogen, southeast Australia: Economic Geology, v. 100, p. 385–398, https://doi.org/10.2113/gsecongeo.100.2.385.

Bloem, E.J.M., Dalstra, H.J., Groves, D.I., and Ridley, J.R., 1994, Metamorphic and structural setting of Archaean amphibolite-hosted gold deposits near Southern Cross, Southern Cross Province, Yilgarn Block, Western Australia: Ore Geology Reviews, v. 9, p. 183–208, https://doi.org/10.1016/0169-1368(94)90005-1.

Brugger, J., Lahaye, Y., Costa, S., Lambert, D., and Bateman, R., 2000, Inhomogeneous distribution of REE in scheelite and dynamics of Archaean hydrothermal systems (Mt. Charlotte and Drysdale gold deposits, Western Australia): Contributions to Mineralogy and Petrology, v. 139, p. 251–264, https://doi.org/10.1007/s004100000135.

Cao, M.J., Zhou, Q.F., Qin, K.Z., Tang, D.M., and Evans, N.J., 2013, The tetrad effect and geochemistry of apatite from the Altay Koktokay No. 3 pegmatite, Xinjiang, China: Implications for pegmatite petrogenesis: Mineralogy and Petrology, v. 107, p. 985–1,005, https://doi.org/10.1007/s00710-013-0270-x.

Cao, M.J., Evans, N.J., Hollings, P., Cooke, D.R., McInnes, B.I.A., and Qin, K.Z., 2021, Apatite texture, composition, and O-Sr-Nd isotope signatures record magmatic and hydrothermal fluid characteristics at the Black Mountain Porphyry Deposit, Philippines: Economic Geology, v. 116, p. 1189–1207, https://doi.org/10.5382/econgeo.4827.

Charvet, J., Shu, L.S., Faure, M., Choulet, F., Wang, B., Lu, H.F., and Breton, N.L., 2010, Structural development of the Lower Paleozoic belt of South China: Genesis of an intracontinental orogen: Journal of Asian Earth Sciences, v. 39, no. 4, p. 309–330, https://doi.org/10.1016/j.jseaes.2010.03.006.

Chen, M., Bagas, L., Liao, X., Zhang, Z., and Li, Q., 2019, Hydrothermal apatite SIMS Th-Pb dating: Constraints on the timing of low-temperature hydrothermal Au deposits in Nibao, SW China: Lithos, v. 324–325, p. 418–428, https://doi.org/10.1016/j.lithos.2018.11.018.

Chen, W.T., Zhou, M.F., and Gao, J.F., 2014, Constraints of Sr isotopic compositions of apatite and carbonates on the origin of Fe and Cu mineralizing fluids in the Lala Fe-Cu-(Mo, LREE) deposit, SW China: Ore Geology Reviews, v. 61, p. 96–106, https://doi.org/10.1016/j.oregeorev.2014.01.008.

Cherniak, D.J., 2006, Pb and rare earth element diffusion in xenotime: Lithos, v. 88, p. 1–14, https://doi.org/10.1016/j.lithos.2005.08.002.

Chu, M.F., Wang, K.L., Griffin, W.L., Chung, S.L., O'Reilly, S.Y., Pearson, N.J., and Iizuka, Y., 2009, Apatite composition: tracing petrogenetic processes in Transhimalayan granitoids: Journal of Petrology, v. 50, p. 1829–1855, https://doi.org/10.1093/petrology/egp054.

Corfu, F., Hanchar, J.M., Hoskin, P.W.O., and Kinny, P., 2003, Atlas of zircon texture: Reviews in Mineralogy and Geochemistry, v. 53, p. 469–500, https://doi.org/10.2113/0530469.

Crawford, A.J., and Doyle, M.G., 2016, Granulite-hosted gold: tectonic setting and lithogeochemistry of the Tropicana deposit, Western Australia: Economic Geology, v, 111, p. 395–420, https://doi.org/10.2113/econgeo.111.2.395.

Creaser, R.A., and Gray, C.M., 1992, Preserved initial $^{87}Sr/^{86}Sr$ in apatite from altered felsic igneous rocks: A case study from the middle Proterozoic of South Australia: Geochimica et Cosmochimica Acta, v. 56, p. 2789–2795, https://doi.org/10.1016/0016-7037(92)90359-Q.

de Melo, R.P., de Oliveira, M.A.F., Goldfarb, R.J., Johnson, C.A., Marsh, E.E., Xavier, R.P., de Oliveria, L.D., and Morgan, L.E., 2022, Early Neoproterozoic gold deposits of the Alto Guaporé Province, Southwestern Amazon Craton, Western Brazil: Economic Geology, v. 117, p. 127–163, https://doi.org/10.5382/econgeo.4852.

Deng, J., and Wang, Q.F., 2016, Gold mineralization in China: Metallogenic provinces, deposit types and tectonic framework: Gondwana Research, v. 36, p. 219–274, https://doi.org/10.1016/j.gr.2015.10.003.

Faure, M., Shu, L.S., Wang, B., Charvet, J., Choulet, F., and Monie, P., 2009, Intracontinental subduction: A possible mechanism for the Early Palaeozoic Orogen of SE China: Terra Nova, v. 21, no. 5, p. 360–368, https://doi.org/10.1111/j.1365-3121.2009.00888.x.

Fox, D.C.M., Spinks, S.C., Barham, M., Kirkland, C.L., Pearce, M.A., Aspandiar, M., Birchall, R., and Mead, E., 2021, Working up an apatite: Enigmatic Mesoarchean hydrothermal Cu-Co-Au mineralization in the Pilbara Craton: Economic Geology, v. 116, p. 1,561–1,573, https://doi.org/10.5382/econgeo.4842.

Frimmel, H.E., 2018, Episodic concentration of gold and ore grade through Earth's history: Earth-Science Reviews, v. 180, p. 148–158, https://doi.org/10.1016/j.earscirev.2018.03.011.

Gaboreau, S., Cuney, M., Quirt, D., Beaufort, D., Patrier, P., and Mathieu, R., 2007, Significance of aluminum phosphate-sulfate minerals associated with U unconformity-type deposits: The Athabasca basin, Canada: The American Mineralogist, v. 92, p. 267–280, https://doi.org/10.2138/am.2007.2277.

Genna, D., Gaboury, D., and Roy, G., 2014, Evolution of a volcanogenic hydrothermal system recorded by the behavior of LREE and Eu: Case study of the Key Tuffite at Bracemac-McLeod deposits, Matagami, Canada: Ore Geology Reviews, v. 63, p. 160–177, https://doi.org/10.1016/j.oregeorev.2014.04.019.

Glodny, J., and Grauert, B., 2009, Evolution of a hydrothermal fluid-rock interaction system as recorded by Sr isotopes: A case study from the Schwarzwald, SW Germany: Mineralogy and Petrology, v. 95, no. 163, https://doi.org/10.1007/s00710-008-0034-1.

Glorie, S., Jepson, G., Konopelko, D., Mirkamalov, R., Meeuws, F., Gilbert, S., Gillespie, J., Collins, A.S., Xiao, W., Dewaele, S., and De Grave, J., 2019, Thermochronological and geochemical footprints of post-orogenic fluid alteration recorded in apatite: Implications for mineralisation in the Uzbek Tian Shan: Gondwana Research, v. 71, p. 1–15, https://doi.org/10.1016/j.gr.2019.01.011.

Goldfarb, R.J., Baker, T., Dube, B., Groves, D.I., Hart, C.J.R., and Gosselin, P., 2005, Distribution, character, and genesis of gold deposits in metamorphic terranes, *in* Hedenquist, J.W., Thompson, J.F.H., Goldfarb, R.J., and Richards, J.P., eds., Economic Geology: One Hundredth Anniversary Volume: Littleton, Colorado, USA, Society of Economic Geologists, p. 407–450, https://doi.org/10.5382/AV100.14.

Goldfarb, R., Qiu, K., Deng, J., Chen, Y., and Yang, L., 2019, Orogenic gold deposits of China: Society of Economic Geology Special Publication, v. 22, p. 263–324.

Groves, D., 1993, The crustal continuum model for late-Archaean lode-gold deposits of the Yilgarn block, Western Australia: Mineralium Deposita, v. 28, p. 366–374, https://doi.org/10.1007/BF02431596.

Groves, D.I., Santosh, M., Deng, J., Wang, Q.F., Yang, L.Q., and Zhang, L., 2019, A holistic model for the origin of orogenic gold deposits and its implications for exploration: Mineralium Deposita, v. 55, p. 275–292, https://doi.org/10.1007/s00126-019-00877-5.

Harlov, D.E., and Förster, H.J., 2003, Fluid-induced nucleation of (Y + REE)- phosphate minerals within apatite: Nature and experiment. Part II. Fluorapatite: The American Mineralogist, v. 88, p. 1209–1229, https://doi.org/10.2138/am-2003-8-905.

Harlov, D.E., Andersson, U.B., Förster, H.J., Nyström, J.O., Dulski, P., and Broman, C., 2002a, Apatite-monazite relations in the Kiirunavaara magnetite-apatite ore, northern Sweden: Chemical Geology, v. 191, p. 47–72, https://doi.org/10.1016/S0009-2541(02)00148-1.

Harlov, D.E., Förster, H.J., and Nijland, T.G., 2002b, Fluid-induced nucleation of (Y + REE)-phosphate minerals within apatite: Nature and experiment. Part I. Chlorapatite: The American Mineralogist, v. 87, p. 245–261, https://doi.org/10.2138/am-2002-2-306.

Hazarika, P., Mishra, B., and Pruseth, K.L., 2016, Scheelite, apatite, calcite and tourmaline compositions from the late Archean Hutti orogenic gold deposit: Implications for analogous two stage ore fluids: Ore Geology Reviews, v. 72, p. 989–1003, https://doi.org/10.1016/j.oregeorev.2015.09.004.

Henrichs, I.A., O'Sullivan, C., Chew, D.M., Mark, C., Babechuk, M.G., and Emo, R., 2018, The trace element and U-Pb systematics of metamorphic apatite: Chemical Geology, v. 483, p. 218–238, https://doi.org/10.1016/j.chemgeo.2017.12.031.

Huang, C.P., 2001, Research on the metallogenic characteristics and forecast of gold deposits in Fujian Province, China [Ph.D. thesis] [in Chinese with English abstract]: China University of Geosciences (Beijing), 135 p.

Jones, R.H., McCubbin, F.M., Dreeland, L., Guan, Y., Burger, P.V., and Shearer, C.K., 2014, Phosphate minerals in LL chondrites: A record of the action of fluids during metamorphism on ordinary chondrite parent bodies: Geochimica et Cosmochimica Acta, v. 132, p. 120–140, https://doi.org/10.1016/j.gca.2014.01.027.

Kirkland, C.L., Yakymchuk, C., Szilas, K., Evans, N., Hollis, J., McDonald, B., and Gardiner, N.J., 2018, Apatite: A U-Pb thermochronometer or geochronometer?: Lithos, v. 318–319, p. 143–157, https://doi.org/10.1016/j.lithos.2018.08.007.

Kositcin, N., McNaughton, N.J., Griffin, B.J., Fletcher, I.R., Groves, D.I., and Rasmussen, B., 2003, Textural and geochemical discrimination between xenotime of different origin in the Archaean Witwatersrand Basin,

South Africa: Geochimica et Cosmochimica Acta, v. 67, p. 709–731, https://doi.org/10.1016/S0016-7037(02)01169-9.

Kou, G., Feng, J., and Wei, M., 2016, The geological features and prospecting criteria of Shuangqishan Au deposit in Fujian [in Chinese with English abstract]: Geology of Yunnan, v. 35, p. 98–102.

Kozlik, M., Gerdes, A., and Raith, J.G., 2016, Strontium isotope systematics of scheelite and apatite from the Felbertal tungsten deposit, Austria: Results of in-situ LA-MC-ICP-MS analysis: Mineralogy and Petrology, v. 110, p. 11–27, https://doi.org/10.1007/s00710-015-0416-0.

Krneta, S., Ciobanu, C.L., Cook, N.J., Ehrig, K., and Kontonikas-Charos, A., 2016, Apatite at Olympic Dam, South Australia: A petrogenetic tool: Lithos, v. 262, p. 470–485, https://doi.org/10.1016/j.lithos.2016.07.033.

Kusebauch, C., John, T., Whitehouse, M.J., and Engvik, A.K., 2015, Apatite as probe for the halogen composition of metamorphic fluids (Bamble Sector, SE Norway): Contributions to Mineralogy and Petrology, v. 170, p. 34, https://doi.org/10.1007/s00410-015-1188-6.

Large, R.R., Danyushevsky, L., Hollitt, C., Maslennikov, V., Meffre, S., Gilbert, S., Bull, S., Scott, R., Emsbo, P., Thomas, H., Singh, B., and Foster, J., 2009, Gold and trace element zonation in pyrite using a laser imaging technique: Implications for the timing of gold in orogenic and Carlin-style sediment-hosted gold deposits: Economic Geology, v. 104, p. 635–668, https://doi.org/10.2113/gsecongeo.104.5.635.

Lawrence, D.M., Treloar, P.J., Rankin, A.H., Harbindge, P., and Holiday, J., 2013, The geology and mineralogy of the Loulo mining district, Mali, West Africa: Evidence for two distinct styles of orogenic gold mineralization: Economic Geology, v. 108, p. 199–227, https://doi.org/10.2113/econgeo.108.2.199.

Li, N.S., 2010, Shuangqishan gold deposit geological features and metallogenic prognosis of deep edge [in Chinese with English abstract]: Kexue Jishu Yu Gongcheng, v. 20, p. 4905–4912.

Li, S.N., Ni, P., Bao, T., Li, C.Z., Xiang, H.L., Wang, G.G., Huang, B., Chi, Z., Dai, C.Z., and Ding, J.Y., 2018a, Geology, fluid inclusion, and stable isotope systematics of the Dongyang epithermal gold deposit, Fujian Province, southeast China: Implications for ore genesis and mineral exploration: Journal of Geochemical Exploration, v. 195, p. 16–30, https://doi.org/10.1016/j.gexplo.2018.02.009.

Li, W., Xie, G.Q., Mao, J.W., Zhang, Z.Y., Fu, B., and Lu, S., 2018b, Muscovite $^{40}Ar/^{39}Ar$ and in situ sulfur isotope analyses of the slate-hosted Gutaishan Au-Sb deposit, South China: Implications for possible Late Triassic magmatic-hydrothermal mineralization: Ore Geology Reviews, v. 101, p. 839–853, https://doi.org/10.1016/j.oregeorev.2018.08.006.

Li, W., Cook, N.J., Xie, G.Q., Mao, J.W., Ciobanu, C.L., and Fu, B., 2021a, Complementary textural, trace element, and isotopic analyses of sulfides constrain ore-forming processes for the slate-hosted Yuhengtang Au deposit, South China: Economic Geology, v. 116, p. 1825–1848, https://doi.org/10.5382/econgeo.4847.

Li, W.T., Jiang, S.Y., Fu, B., Liu, D.L., and Xiong, S.F., 2021b, Zircon Hf-O isotope and magma oxidation state evidence for the origin of Early Cretaceous granitoids and porphyry Mo mineralization in the Tongbai-Hong'an-Dabie orogens, Eastern China: Lithos, v. 389–399, https://doi.org/10.1016/j.lithos.2021.106281.

Li, W., Xie, G.Q., Mao, J.W., Cook, N.J., Wei, H.T., Ji, Y.H., and Fu, B., 2022a, Precise age constraints for the Woxi Au-Sb-W deposit, South China: Economic Geology, https://doi.org/10.5382/econgeo.4971, (in press).

Li, X.C., Harlov, D.E., Zhou, M.F., and Hu, H., 2022b, Metasomatic modification of Sr isotopes in apatite as a function of fluid chemistry: Geochimica et Cosmochimica Acta, v. 323, p. 123–140, https://doi.org/10.1016/j.gca.2022.02.025.

Li, Z.X., and Li, X.H., 2007, Formation of the 1300-km-wide intracontinental orogen and postorogenic magmatic province in Mesozoic South China: A flat-slab subduction model: Geology, v. 35, p. 179–182, https://doi.org/10.1130/G23193A.1.

Li, Z.X., Li, X.H., Wartho, J.A., Clark, C., Li, W.X., Zhang, C.L., and Bao, C.M., 2010, Magmatic and metamorphic events during the early Paleozoic Wuyi-Yunkai orogeny, southeastern South China: New age constraints and pressure-temperature conditions: Geological Society of America Bulletin, v. 122, p. 772–793, https://doi.org/10.1130/B30021.1.

Liu, M.Y., Zhou, M.F., Su, S.G., and Chen, X.G., 2021, Contrasting geochemistry of apatite from peridotites and sulfide ores of the Jinchuan Ni-Cu sulfide deposit, NW China: Economic Geology, v. 116, p. 1073–1092, https://doi.org/10.5382/econgeo.4817.

Liu, W., Mei, Y., Etschmann, B., Brugger, J., Pearce, M., Ryan, C.G., Borg, S., Wykes, J., Kappen, P., Paterson, D., Bosenberg, U., Garrevoet, J., Moorhead, G., and Falkenberg, G., 2017, Arsenic in hydrothermal apatite: Oxidation state, mechanism of uptake, and comparison between experiments and nature: Geochimica et Cosmochimica Acta, v. 196, p. 144–159, https://doi.org/10.1016/j.gca.2016.09.023.

Lüders, V., Romer, R., Gilg, H.A., Bodnar, R.J., Pettke, T., and Misantoni, D., 2009, A geochemical study of the Sweet Home Mine, Colorado Mineral Belt, USA: Hydrothermal fluid evolution above a hypothesized granite cupola: Mineralium Deposita, v. 44, p. 415–434, https://doi.org/10.1007/s00126-008-0221-3.

Ma, Y., Jiang, S.Y., Frimmel, H.E., Xiong, S.F., Zhu, L.Y., and Chen, R.S., 2021, Early Paleozoic Orogenic Gold Deposit in the Cathaysia Block, China: A first example from the Shuangqishan Deposit: Gondwana Research, v. 91, p. 231–253, https://doi.org/10.1016/j.gr.2020.11.014.

Ma, Y., Jiang, S.Y., Frimmel, H.E., Duan, R.C., Zhu, L.Y., and Chen, R.S., 2022a, Age and fluid source of the subvolcanic Zhaiping Ag-Pb-Zn deposit in the eastern Cathaysia Block (Fujian Province, Southeastern China): Mineralium Deposita, v. 57, p. 439–454, https://doi.org/10.1007/s00126-021-01073-0.

Ma, Y., Jiang, S.Y., and Frimmel, H.E., 2022b, Metallogeny of the Late Jurassic Qiucun epithermal gold deposit in southeastern China: Constraints from geochronology, fluid inclusions, and H-O-C-Pb isotopes: Ore Geology Reviews, v. 142, https://doi.org/10.1016/j.oregeorev.2021.104688.

Ma, Y., Jiang, S.Y., and Frimmel, H.E., 2022c, Deciphering multiple ore-forming processes of the Shuangqishan orogenic gold deposit, Southeast China by *in situ* analysis of pyrite: Ore Geology Reviews, v. 142, https://doi.org/10.1016/j.oregeorev.2022.104730.

Malarkey, J., Pearson, D.G., Kjarsgaard, B.A., Davidson, J.P., Nowell, G.M., Ottley, C.J., and Stammer, J., 2010, From source to crust: Tracing magmatic evolution in a kimberlite and a melilitite using microsample geochemistry: Earth and Planetary Science Letters, v. 299, p. 80–90, https://doi.org/10.1016/j.epsl.2010.08.020.

Mao, M., Rukhlov, A.S., Rowins, S.M., Spence, J., and Coogan, L.A., 2016, Apatite trace element compositions: A robust new tool for mineral exploration: Economic Geology, v. 111, p. 1187–1222, https://doi.org/10.2113/econgeo.111.5.1187.

McDonough, W.F., and Sun, S.-S., 1995, The composition of the earth: Chemical Geology, v. 120, p. 223–253, https://doi.org/10.1016/0009-2541(94)00140-4.

McFarlane, C.R.M., Mavrogenes, J., Lentz, D., King, K., Allibone, A., and Holcombe, R., 2011, Geology and intrusion-related affinity of the Morila gold mine, Southeast Mali: Economic Geology, v. 106, p. 727–750, https://doi.org/10.2113/econgeo.106.5.727.

Ni, P., Wang, G.G., Chen, H., Xu, Y.F., Guan, S.J., Pan, J.Y., and Li, L., 2015, An Early Paleozoic orogenic gold belt along the Jiang-Shao Fault, South China: Evidence from fluid inclusions and Rb-Sr dating of quartz in the Huangshan and Pingshui deposits: Journal of Asian Earth Sciences, v. 103, p. 87–102, https://doi.org/10.1016/j.jseaes.2014.11.031.

Ohmoto, H., 1972, Systematics of sulfur and carbon isotopes in hydrothermal ore deposits: Economic Geology, v. 67, p. 551–578, https://doi.org/10.2113/gsecongeo.67.5.551.

Pan, Y., and Fleet, M.E., 2002, Compositions of the apatite-group minerals: Substitution mechanisms and controlling factors: Reviews in Mineralogy and Geochemistry, v. 48, p. 13–49, https://doi.org/10.2138/rmg.2002.48.2.

Palma, G., Barra, F., Reich, M., Valencia, V., Simon, A.C., Vervoort, J., Leisen, M., and Romero, R., 2019, Halogens, trace element concentrations, and Sr-Nd isotopes in apatite from iron oxide-apatite (IOA) deposits in the Chilean iron belt: Evidence for magmatic and hydrothermal stages of mineralization: Geochimica et Cosmochimica Acta, v. 246, p. 515–540, https://doi.org/10.1016/j.gca.2018.12.019.

Peng, B., and Frei, R., 2004, Nd-Sr-Pb isotopic constraints on metal and fluid sources in W-Sb-Au mineralization at Woxi and Liaojiaping (Western Hunan, China): Mineralium Deposita, v. 39, p. 313–327, https://doi.org/10.1007/s00126-004-0409-0.

Pitcairn, I.K., Leventis, N., Beaudoin, G., Faure, S., Guilmette, C., and Dubé, B., 2021, A metasedimentary source of gold in Archean orogenic gold deposits: Geology, v. 49, p. 862–866, https://doi.org/10.1130/G48587.1.

Pitcairn, I.K., Teagle, D.A.H., Craw, D., Olivo, G.R., Kerrich, R., and Brewer, T.S., 2006, Sources of metals and fluids in orogenic gold deposits: Insights from the Otago and Alpine Schists, New Zealand: Economic Geology, v. 101, p. 1525–1546, https://doi.org/10.2113/gsecongeo.101.8.1525.

Putnis, A., 2002, Mineral replacement reactions: From macroscopic observations to microscopic mechanisms: Mineralogical Magazine, v. 66, p. 689–708, https://doi.org/10.1180/0026461026650056.

Qu, P., Yang, W.B., Niu, H.C., Li, N.B., and Wu, D., 2022, Apatite fingerprints on the magmatic-hydrothermal evolution of the Daheishan giant porphyry Mo deposit, NE China: Geological Society of America Bulletin, v. 134, p. 1863–1876, https://doi.org/10.1130/B36093.1.

Robert, F., and Brown, A., 1986, Archean gold-bearing quartz veins at the Sigma Mine, Abitibi greenstone belt, Quebec: Part II, Vein paragenesis and hydrothermal alteration: Economic Geology, v. 81, p. 593–616, https://doi.org/10.2113/gsecongeo.81.3.593.

Roberts, S., Palmer, M.R., and Waller, L., 2006, Sm-Nd and REE characteristics of tourmaline and scheelite from the Björkdal gold deposit, northern Sweden: Evidence of an intrusion-related gold deposit?: Economic Geology, v. 101, p. 1415–1425, https://doi.org/10.2113/gsecongeo.101.7.1415.

Scanlan, E.M., Scott, J.M., Wilson, V.J., Stirling, C.H., Reid, M.R., and Le Roux, P.J., 2018, In situ $^{87}Sr/^{86}Sr$ of scheelite and calcite reveals proximal and distal fluid-rock interaction during orogenic W-Au mineralization, Otago Schist, New Zealand: Economic Geology, v. 113, p. 1571–1586, https://doi.org/10.5382/econgeo.2018.4603.

Sciuba, M., and Beaudoin, G., 2021, Texture and trace element composition of rutile in orogenic gold deposits: Economic Geology, v. 116, p. 1865–1892, https://doi.org/10.5382/econgeo.4857.

Shelton, K.L., McMenamy, T.A., van Hees, E.H.P., and Flack, H., 2004, Deciphering the complex fluid history of a greenstone-hosted gold deposit: Fluid inclusion and stable isotope studies of the Giant Mine, Yellowknife, Northwest Territories, Canada: Economic Geology, v. 99, p. 1643–1663, https://doi.org/10.2113/gsecongeo.99.8.1643.

Sverjensky, D.A., 1984, Europium redox equilibria in aqueous solution: Earth and Planetary Science Letters, v. 67, p. 70–78, https://doi.org/10.1016/0012-821X(84)90039-6.

Taylor, R.D., Goldfarb, R.J., Monecke, T., Fletcher, I.R., Cosca, M.A., and Kelley, N.M., 2015, Application of U-Th-Pb phosphate geochronology to young orogenic gold deposits: New age constraints on the formation of the Grass Valley gold district, Sierra Nevada foothills province, California: Economic Geology, v. 110, p. 1313–1337, https://doi.org/10.2113/econgeo.110.5.1313.

Taylor, R.D., Monecke, T., Reynolds, T.J., and Monecke, J., 2021, Paragenesis of an orogenic gold deposit: New insights on mineralizing processes at the Grass Valley District, California: Economic Geology, v. 116, p. 323–356, https://doi.org/10.5382/econgeo.4794.

Thomas, H.V., Large, R.R., Bull, S.W., Maslennikov, V., Berry, R.F., Fraser, R., Froud, S., and Moye, R., 2011, Pyrite and pyrrhotite textures and composition in sediments, laminated quartz veins, and reefs at Bendigo gold mine, Australia: Insights for ore genesis: Economic Geology, v. 106, p. 1–31, https://doi.org/10.2113/econgeo.106.1.1.

Tomkins, A.G., 2010, Windows of metamorphic sulfur liberation in the crust: Implications for gold deposit genesis: Geochimica et Cosmochimica Acta, v. 74, p. 3246–3259, https://doi.org/10.1016/j.gca.2010.03.003.

Wan, Y.S., Liu, D.Y., Xu, M.H., Zhuang, J.M., Song, B., Shi, Y.R., and Du, L.L., 2007, SHRIMP U-Pb zircon geochronology and geochemistry of metavolcanic and metasedimentary rocks in Northwestern Fujian, Cathaysia block, China: Tectonic implications and the need to redefine lithostratigraphic units: Gondwana Research, v. 12, p. 166–183, https://doi.org/10.1016/j.gr.2006.10.016.

Wang, J., and Li, Z.X., 2003, History of Neoproterozoic rift basins in South China: Implications for Rodinia breakup: Precambrian Research, v. 122, p. 141–158, https://doi.org/10.1016/S0301-9268(02)00209-7.

Watson, E.B., and Green, T.H., 1981, Apatite/liquid partition coefficients for the rare earth elements and strontium: Earth and Planetary Science Letters, v. 56, p. 405–421, https://doi.org/10.1016/0012-821X(81)90144-8.

Williams, N.C., 2007, The role of decarbonization and structure in the Callie gold deposit, Tanami Region of northern Australia: Mineralium Deposita, v. 42, p. 65–87, https://doi.org/10.1007/s00126-006-0096-0.

Wu, J.S., 2002, Ore-controlling structure characteristics and metallogenic prediction of Xiaoban gold ore field, Youxi, Fujian [Ph.D. thesis] [in Chinese with English abstract]: China University of Geosciences (Beijing), 106 p.

Xiao, B., and Chen, H.Y., 2020, Elemental behavior during chlorite alteration: new insights from a combined EMPA and LA-ICPMS study in porphyry Cu systems: Chemical Geology, v. 543, https://doi.org/10.1016/j.chemgeo.2020.119604.

Xu, D., Deng, T., Chi, G., Wang, Z., Zou, F., Zhang, J., and Zou, S., 2017, Gold mineralization in the Jiangnan Orogenic Belt of South China: Geological, geochemical and geochronological characteristics, ore deposit-type and geodynamic setting: Ore Geology Reviews, v. 88, p. 565–618, https://doi.org/10.1016/j.oregeorev.2017.02.004.

Xue, Y., Campbell, I., Ireland, T.R., Holden, P., and Armstrong, R., 2013, No mass-independent S isotope fractionation in auriferous fluids supports a magmatic origin for Archean gold deposits: Geology, v. 41, p. 791–794, https://doi.org/10.1130/G34186.1.

Ying, Y.C., Chen, W., Simonetti, A., Jiang, S.Y., and Zhao, K.D., 2020, Significance of hydrothermal reworking for REE mineralization associated with carbonatite: Constraints from in situ trace element and C-Sr isotope study of calcite and apatite from the Miaoya carbonatite complex (China): Geochimica et Cosmochimica Acta, v. 280, p. 340–359, https://doi.org/10.1016/j.gca.2020.04.028.

Yuan, H.X., and Chen, H., 2015, Prospecting progress and metallogenic characteristics of gold in Dehua area of Fujian Province [in Chinese]: Acta Mineralogica Sinica, v. 35, p. 1055–1055.

Yuan, Z.X., Wu, L.S., Zhang, Z.Q., and Ye, X.J., 1991, Study on Sm-Nd and Rb-Sr isotopic age of the Mayuan Group in Northern Fujian [in Chinese with English abstract]: Acta Petrologica et Mineralogica, v. 10, p. 128–132.

Zeng, L.P., Zhao, X.F., Li, X.C., Hu, H., and McFarlane, C., 2016, In situ elemental and isotopic analysis of fluorapatite from the Taocun magnetite-apatite deposit, Eastern China: Constraints on fluid metasomatism: The American Mineralogist, v. 101, p. 2468–2483, https://doi.org/10.2138/am-2016-5743.

Zhang, D., Wu, G.G., Peng, R.M., Wu, J.S., Di, Y.J., Zhang, X.X., and Wang, Q.F., 2005, Paleotectonic setting of the Dongyan Formation of the Mamianshan Group in central Fujian Province, southeast China [in Chinese with English abstract]: Earth Science Frontiers, v. 12, p. 310–320.

Zhang, F.H., Li, W.B., White, N.C., Zhang, L.J., Qian, X.Y., and Yao, Z.W., 2020, Geochemical and isotopic study of metasomatic apatite: Implications for gold mineralization in Xindigou, northern China: Ore Geology Reviews, v. 127, https://doi.org/10.1016/j.oregeorev.2020.103853.

Zhang, J., Huang, W.T., Wu, J., Liang, H.Y., and Liu, S.P., 2021, Geological implications of apatite within the granite-related Jiepai W-(Cu) deposit, Guangxi, South China: Ore Geology Reviews, v. 139, https://doi.org/10.1016/j.oregeorev.2021.104548.

Zhang, L., Yang, L.Q., Groves, D.I., Sun, S.C., Liu, Y., Wang, J.Y., Li, R.H., Wu, S.G., Gao, L., Guo, J.L., Chen, X.G., and Chen, J.H., 2019, An overview of timing and structural geometry of gold, gold-antimony and antimony mineralization in the Jiangnan Orogen, southern China: Ore Geology Reviews, v. 115, https://doi.org/10.1016/j.oregeorev.2019.103173.

Zhang, Q., Jiang, Y.H., Wang, G.C., Liu, Z., Ni, C.Y., and Qing, L., 2015, Origin of Silurian gabbros and I-type granites in central Fujian, SE China: Implications for the evolution of the early Paleozoic orogen of South China: Lithos, v. 216–217, p. 285–297, https://doi.org/10.1016/j.lithos.2015.01.002.

Zhao, J.H., Zhou, M.F., Yan, D.P., Zheng, J.P., and Li, J.W., 2011, Reappraisal of the ages of Neoproterozoic strata in South China: No connection with the Grenvillian orogeny: Geology, v. 39, p. 299–302, https://doi.org/10.1130/G31701.1.

Zhao, X.F., Zhou, M.F., Gao, J.F., Li, X.C., and Li, J.W., 2015, In situ Sr isotope analysis of apatite by LA-MC-ICPMS: Constraints on the evolution of ore fluids of the Yinachang Fe-Cu-REE deposit, Southwest China: Mineralium Deposita, v. 50, p. 871–884, https://doi.org/10.1007/s00126-015-0578-z.

Zheng, J.H., Shen, P., and Feng, W.Y., 2022, Hydrothermal apatite record of ore-forming processes in the Hatu orogenic gold deposit, West Junggar, Northwest China: Contributions to Mineralogy and Petrology, v. 177, no. 27, https://doi.org/10.1007/s00410-022-01893-x.

Zhou, X.M., Sun, T., Shen, W.Z., Shu, L.S., and Niu, Y.L., 2006, Petrogenesis of Mesozoic granitoids and volcanic rocks in South China: A response to tectonic evolution: Episodes v. 29, p. 26–33, https://doi.org/10.18814/epiiugs/2006/v29i1/004.

Science Editor: Wenjiao Xiao
Associate Editor: Haibo Zou

Manuscript Received 18 June 2022
Revised Manuscript Received 30 September 2022
Manuscript Accepted 17 November 2022

Printed in the USA